Drug Delivery

ISSN: 1071-7544 (Print) 1521-0464 (Online) Journal homepage: www.tandfonline.com/journals/idrd20

Sequential nanotheranostics based on hollow mesoporous silica loaded doxorubicin and seed kernel extract from *Mangifera indica* L. as adjuvant therapy against hepatocellular carcinoma

Arunsajee Sae-be , Jiraporn Leanpolchareanchai , Piyaporn Plommaithong , Apichat Chatsukit , Shanapa Ratthanakanungthum , Kuntida Wongwattanasan , Tomoki Ota , Sarunyakorn Raowong , Pongtip Sithisarn , Savita Chewchinda , Parichart Naruphontjirakul , Teerasit Termsaithong , Thana Sutthibutpong , Varaporn Buraphacheep Junyaprasert , Khanit Sa-ngiamsuntorn , Rapepol Bavovada , Pimolpan Pithayanukul , Alexandra E. Porter & Pakatip Ruenraroengsak

To cite this article: Arunsajee Sae-be , Jiraporn Leanpolchareanchai , Piyaporn Plommaithong , Apichat Chatsukit , Shanapa Ratthanakanungthum , Kuntida Wongwattanasan , Tomoki Ota , Sarunyakorn Raowong , Pongtip Sithisarn , Savita Chewchinda , Parichart Naruphontjirakul , Teerasit Termsaithong , Thana Sutthibutpong , Varaporn Buraphacheep Junyaprasert , Khanit Sa-ngiamsuntorn , Rapepol Bavovada , Pimolpan Pithayanukul , Alexandra E. Porter & Pakatip Ruenraroengsak (2025) Sequential nanotheranostics based on hollow mesoporous silica loaded doxorubicin and seed kernel extract from *Mangifera indica* L. as adjuvant therapy against hepatocellular carcinoma, Drug Delivery, 32:1, 2559838, DOI: 10.1080/10717544.2025.2559838

To link to this article: https://doi.org/10.1080/10717544.2025.2559838

© 2025 The Author(s). Published by Informa UK Limited, trading as Taylor & Francis Group.

View supplementary material

Published online: 22 Sep 2025.

Submit your article to this journal

Article views: 184

View related articles

View Crossmark data

Full Terms & Conditions of access and use can be found at
https://www.tandfonline.com/action/journalInformation?journalCode=idrd20

DRUG DELIVERY
2025, VOL. 32, NO. 1, 2559838
https://doi.org/10.1080/10717544.2025.2559838

Taylor & Francis
Taylor & Francis Group

RESEARCH ARTICLE

OPEN ACCESS Check for updates

Sequential nanotheranostics based on hollow mesoporous silica loaded doxorubicin and seed kernel extract from *Mangifera indica* L. as adjuvant therapy against hepatocellular carcinoma

Arunsajee Sae-be[a,b], Jiraporn Leanpolchareanchai[a], Piyaporn Plommaithong[a], Apichat Chatsukit[a], Shanapa Ratthanakanungthum[a], Kuntida Wongwattanasan[a], Tomoki Ota[a,c], Sarunyakorn Raowong[a,b], Pongtip Sithisarn[d], Savita Chewchinda[e], Parichart Naruphontjirakul[f], Teerasit Termsaithong[g,h], Thana Sutthibutpong[h], Varaporn Buraphacheep Junyaprasert[a], Khanit Sa-ngiamsuntorn[b,i], Rapepol Bavovada[j], Pimolpan Pithayanukul[a], Alexandra E. Porter[k] and Pakatip Ruenraroengsak[a,b]

[a]Department of Pharmacy, Faculty of Pharmacy, Mahidol University, Rajathevi, Bangkok, Thailand; [b]Centre of Molecular Targeting and Integrated Drug Development (CMT-IDD), Faculty of Pharmacy, Mahidol University, Rajathevi, Bangkok, Thailand; [c]The School of Pharmaceutical Science, Kyushu University, Fukuoka, Japan; [d]Department of Pharmacognosy, Faculty of Pharmacy, Mahidol University, Rajathevi, Bangkok, Thailand; [e]Department of Food Chemistry, Faculty of Pharmacy, Mahidol University, Rajathevi, Bangkok, Thailand; [f]Biological Engineering Program, Faculty of Engineering, King Mongkut's University of Technology Thonburi, Bangkok, Thailand; [g]Learning Institute, King Mongkut's University of Technology Thonburi, Bangkok, Thailand; [h]Theoretical and Computational Physics Group (TCP), Center of Excellence in Theoretical and Computational Science (TaCS-CoE), Faculty of Science, King Mongkut's University of Technology Thonburi, Bangkok, Thailand; [i]Department of Biochemistry, Faculty of Pharmacy, Mahidol University, Rajathevi, Bangkok, Thailand; [j]Department of Pharmacognosy and Pharmaceutical Botany, Faculty of Pharmaceutical Sciences, Chulalongkorn University, Pathumwan, Bangkok, Thailand; [k]Department of Materials and London Centre for Nanotechnology, Imperial College London, London, United Kingdom

ABSTRACT

Mango seed kernel extract (MSKE) and its phytochemical compositions were investigated for their anticancer activities and synergistic effects with doxorubicin (DOX) against hepatocellular carcinoma (HCC) in both 2D and 3D culture models. Molecular docking studies were conducted to elucidate the mechanisms of DOX, MSKE, and major phytochemical components against overexpressed HCC-related proteins. Co-delivery of DOX and MSKE demonstrated significant synergistic anticancer activity in both models. A sequential nanotheranostic platform (SNP), consisting of MSKE encapsulated aminated hollow mesoporous silica nanoparticles capped with graphene quantum dots (GQD-MSKE-NH_2HMSNs) and DOX encapsulated HMSNs (DOX-HMSNs), was synthesized for HCC treatment. GQD conjugation allowed real-time cellular tracking and photothermal therapy (PTT). The SNP exhibited particle sizes of 96.12 ± 5.12 nm for GQD-MSKE-NH_2HMSNs and 94.99 ± 6.30 nm for DOX-HMSNs, both with positive surface charges. Encapsulation efficiency (%EE) and loading capacity (%LC) of GQD-MSKE-NH_2HMSNs were 95.50 ± 0.20% and 46.72 ± 1.14%, respectively, while DOX-HMSNs achieved 96.42 ± 2.48 %EE and 29.0 ± 0.70 %LC. GQD-MSKE-NH_2HMSNs provided PTT and disrupted the tumor microenvironment, collagen type 1, thereby enhancing the penetration of GQD-MSKE-NH_2HMSNs in 3D-HCC spheroids. In parallel, DOX-HMSNs exhibited a pH-responsive drug release behavior, allowing controlled DOX delivery in the acidic tumor area. Therefore, the SNP demonstrated significantly higher anticancer efficacy than the combination of MSKE and DOX at equivalent concentrations and provided the synergistic effect of the triple combination therapy (herbal adjuvant, PTT and chemotherapy) against HCC.

ARTICLE HISTORY
Received 18 April 2025
Revised 7 August 2025
Accepted 5 September 2025

KEYWORDS
Hepatocellular carcinoma; hollow mesoporous silica nanoparticle; sequential-delivery system; nanotheranostics; *Mangifera indica*; combination therapy

1. Introduction

Liver cancer was the third leading cause of cancer-related deaths worldwide in 2022, accounting for approximately 7.8% (>750,000 cases) of all cancer mortalities (Ferlay et al. 2022). Hepatocellular carcinoma (HCC), the most prevalent form of primary liver cancer, represents over 80% of all liver cancer

CONTACT Pakatip Ruenraroengsak pakatip.rue@mahidol.ac.th Department of Pharmacy, Faculty of Pharmacy, Mahidol University, Rajathevi, Bangkok, 10400 Thailand.

Supplemental data for this article can be accessed online at https://doi.org/10.1080/10717544.2025.2559838.

© 2025 The Author(s). Published by Informa UK Limited, trading as Taylor & Francis Group.
This is an Open Access article distributed under the terms of the Creative Commons Attribution-NonCommercial License (http://creativecommons.org/licenses/by-nc/4.0/), which permits unrestricted non-commercial use, distribution, and reproduction in any medium, provided the original work is properly cited. The terms on which this article has been published allow the posting of the Accepted Manuscript in a repository by the author(s) or with their consent.

cases. The high incidence of death by HCC is associated with poor prognosis because the early diagnosis and treatment have not been fully developed (Yang et al. 2019; Singal et al. 2023). Notably, more than 50% of the new cases have been diagnosed as the intermediate to advanced stages with a 5-year survival rate of approximately 1–1.5 years (Llovet et al. 2021). The treatments including tumor removal, local ablation, chemotherapy, and immunological therapy have been the current first-line treatment in HCC patients, depending on HCC stages. Conventional chemotherapy drugs such as doxorubicin (DOX) have been studied for advanced HCC treatment over the past decade. However, the objective response rate of DOX was around 10% with an incidence of dose-dependent chronic cardiomyopathy and high development of drug resistance (EASL, 2018). In recent years, combination therapies have been explored to enhance therapeutic outcomes while minimizing toxicity related side effects (Yang et al. 2019; Singal et al. 2023).

Natural products are valuable resources for the discovery of new anticancer drugs. In addition to their direct cytotoxic effects, they are increasingly recognized for their potential as adjuvants in cancer chemotherapy, owing to their ability to mitigate chemoresistance and reduce the adverse effects of conventional anticancer agents (Lin et al. 2020). *Mangifera indica* L. (*M. indica*), commonly known as mango, contains several bioactive phytochemicals such as polyphenols, and terpenoids, depending on plant parts. Extracts from *M. indica* have demonstrated diverse biological and pharmacological properties, including antioxidants, anti-inflammatory, antimicrobial, hepatoprotective, and anticancer activities (Nithitanakool et al. 2009; Mirza et al. 2021). Notably, the ethanolic extract of mango seed kernels (MSKE), a by-product of the food industry, has shown the ability to induce apoptosis in breast cancer (MCF-7) cells, *in vitro* (Abdullah et al. 2015). Furthermore, *in vitro* antiproliferation effects of the MSKE were reported against breast cancer cells (MDA-MB-231), liver cancer (HepG2), and leukemia (HL-60) cells. These anticancer activities are believed to be largely attributed to penta-O-galloyl-glucoside (PGG) and its analogs with different galloyl groups (gallotannins) (Luo et al. 2014). It would be of interest to compare the anticancer activity between the MSKE and PGG, as well as to evaluate the potential synergistic effects between MSKE or PGG and chemotherapeutic agents, in order to better understand their combined mechanisms against HCC.

Another combination that has gained considerable attention is chemotherapy coupled with photothermal therapy (PTT) because the PTT enhances the sensitivity of cancer cells to chemotherapeutic drugs by inducing DNA damage and mediating the tumor microenvironment (TME) (Issels 2008). The TME acts as a physical barrier that plays a critical role in limiting anticancer drug penetration (He et al. 2023). The photothermal treatment could decrease the stiffness of extracellular matrix (ECM) in TME, and increase vascular permeability, consequently, escalating drug penetration at the tumor side (Marangon et al. 2017). A triple combination therapy between herbal adjuvants, PTT, and chemotherapy may offer enhanced anticancer efficacy against HCC. In this study, a novel sequential nanotheranostic platform (SNP) based on a passive target strategy of therapeutic nanocarriers was designed to minimize side effects obtained from simultaneous delivery and to enhance the access of drug molecules to tumor sites (Shim et al. 2017; Huang et al. 2022).

Hollow mesoporous silica nanoparticles (HMSNs) have been broadly explored as nanocarriers for both hydrophilic and hydrophobic drugs due to their biocompatibility, biodegradability, high drug-loading capacity, versatile surface modification and pH-responsive drug release (Chen et al. 2014; Kong et al. 2017). Drug release from HMSNs can be triggered by both internal and external stimuli, and their surfaces can be engineered to facilitate controlled release, imaging, and targeted delivery (Chen et al. 2014). Graphene quantum dots (GQDs), biocompatible carbon-based nanomaterials, possess unique optical and physicochemical properties, making them suitable for PTT in biomedical applications (Chong et al. 2014). GQDs can efficiently convert near-infrared (NIR) light into heat through non-radiative relaxation and exhibit tunable fluorescence due to their tunable bandgap, surface imperfections, and zigzag edges (Dar et al. 2023). The surface capping of GQDs onto MSNs and HMSNs facilitates synergistic chemo-photothermal therapy while this also offers fluorescence imaging facility (Chen et al. 2014; Yao et al. 2017). Extending this strategy, the surface modification of HMSNs with GQDs can be further developed into a novel SNP for integrated combination cancer therapy.

In this study, the optimal doses of MSKE and PGG providing synergistic effects with DOX were first identified and compared in both 2D-hepatoma cells (HepG2) and 3D-HepG2 spheroid models. The molecular mechanisms of the major phytochemicals in MSKE including PGG, gallic acid (GA), and methyl gallate (MGA) were revealed using molecular docking with overexpressed target proteins in HCC. The novel SNP integrated a dual-nanocarrier system comprising MSKE-loaded aminated hollow mesoporous silica nanoparticles capped with graphene quantum dots (GQD-MSKE-NH_2HMSNs) and doxorubicin-loaded HMSNs (DOX-HMSNs). This design enabled a sequential delivery strategy that offers triple combination therapy (herbal adjuvant, PTT, and chemotherapy) for the synergistic treatment of HCC. GQD-MSKE-NH_2HMSNs were initially administered to deliver PTT, thereby disrupting the TME and subsequently releasing MSKE into both 2D-HepG2 cultures and the internal core of 3D-HepG2 spheroids. The internalization of GQD-MSKE-NH_2HMSNs could be visualized *via* optical imaging due to the fluorescent properties of GQDs. Finally, DOX was released from DOX-HMSNs in response to the acidic pH in the tumor area. Altogether, this SNP system significantly enhanced anticancer efficacy by the synergistic effect and represents a promising strategy for HCC treatment.

2. Materials and methods

2.1. Materials

Ammonium hydroxide (NH_4OH, 28%–30%), absolute ethanol, cetyltrimethylammonium chloride solution (CTAC, 25% wt. H_2O), sodium carbonate (Na_2CO_3), 37% hydrochloric acid (HCl), tetraethyl orthosilicate (TEOS), triethylamine (TEA), (3-aminopropyl)triethoxysilane (APTES), 1-ethyl-3-(3-dimethylaminopropyl) carbodiimide hydrochloride (EDC), N-hydroxysuccinimide (NHS), trifluoroacetic acid, Folin–Ciocalteu reagent, aluminum chloride ($AlCl_3$), gallic acid (GA), and quercetin were purchased from Sigma-Aldrich (St. Louis, MO, USA). Methanol and acetonitrile (ACN) were purchased from Honeywell (Charlotte, USA). Graphene quantum dots (GQDs, 1 mg/mL) were purchased from Nanjing XFNANO Co. Ltd. (Jiangsu, China). Penta-O-galloyl-glucoside (PGG) was purchased from Biopurify Phytochemicals (Chengdu, China). Doxorubicin hydrochloride (DOX) was purchased from TCI (Tokyo, Japan). HepG2 cells were purchased from ATCC (Manassas, USA) and primary human hepatic stellate cells (HSCs) were purchased from Innoprot (Bizkaia, Spain). Immortalized hepatocyte-like cells (imHCs) were developed by transfecting human mesenchymal stem cells with hTERT plus Bmi-1 and the cells were routinely characterized using our previously published protocol (Sa-Ngiamsuntorn et al. 2011). Cell culture media and supplements (details in cell culture section) were purchased from Cytiva (Massachusetts, USA). Endotoxin assay was purchased from Thermo Fisher Scientific (Massachusetts, USA). Acridine orange (AO) was purchased from Santa Cruze Biotechnology (California, USA). Collagen type 1 (COL1 (ab34710)) and donkey anti-rabbit Alexa Fluor647 were purchased from Abcam (Cambridge, UK). WST-1 and LDH assay kit were purchased from Roche (California, USA). Paraformaldehyde and triton-X were purchased from Merck (Darmstadt, Germany). Bovine serum albumin (BSA) was purchased from Capricorn Scientific (Ebsdorfergrund, Germany). Annexin V, FITC apoptosis detection kit was purchased from Dojindo laboratories (Kumamoto, Japan).

2.2. Mango seed kernel extraction, phytochemical studies, and quality controls

2.2.1. Mango seed kernel extraction

Unripened Thai mango fruits (*Mangifera indica* L. cv. 'Fahlun') were purchased from a local Mahanak market. The fruit specimens were identified by R. Bavovada and a voucher specimen, no. R.B. 20007, was deposited for further reference at the Museum of Natural Medicine, Faculty of Pharmaceutical Sciences, Chulalongkorn University, Bangkok, Thailand. The mango seed kernels were cleaned and dried using a hot air oven at 60 °C for 24 h. The dried mango seed kernels were extracted by 95% v/v ethanol. The ethanol within MSKE was removed *via* rotary evaporation before the freeze-drying process for 48 h and was kept under vacuum at −20 °C until use (Nithitanakool et al. 2009; Leanpolchareanchai et al. 2014; Jiamboonsri et al. 2015). The percentage yield of MSKE was calculated according to its fresh weight.

2.2.2. Assessment of total phenolic compounds by spectrometer

The total phenolic content in MSKE was determined using the Folin-Ciocalteu method (Aryal et al. 2019). Briefly, 8 µL of MSKE solution (0.5 mg/mL) or gallic acid (GA; 0.1–0.75 mg/mL) was mixed with 40 µL of 10% (v/v) Folin-Ciocalteu reagent. Deionized (DI) water, 120 µL, and 7.5% (w/v) Na_2CO_3, 32 µL, were subsequently added to the mixture and incubated in dark condition at room temperature (25 ± 1 °C) for 30 minutes (min). Afterward, the absorbance was measured by a UV-VIS spectrophotometer (Tecan, Switzerland) at the wavelength of 765 nm. The data were extrapolated as g of GA equivalent per 100 g of dry extract (g GAE/100 g extract) with standard deviation (SD).

2.2.3. Assessment of total flavonoid by spectrometer

The total flavonoid contents in MSKE were also quantitatively analyzed using aluminum chloride ($AlCl_3$) method (Aryal et al. 2019). In brief, 0.1 mL of MSKE solution (1 mg/mL) or quercetin (QE; 5–50 µg/mL) was mixed with 0.1 mL of 2% (w/v) $AlCl_3$ solution (Sigma-Aldrich, St. Louis, USA) for 10 min at room temperature (25 ± 1 °C). Then, the absorbance was measured using a UV-VIS spectrophotometer (Tecan, Switzerland) at the wavelength of 415 nm. The outcome data were expressed as g of QE equivalent per g of dry extract (g QE/100 g extract) with SD.

2.2.4. Assessment of PGG by high performance liquid chromatography (HPLC)

The quantitative determination of PGG content in MSKE was performed using HPLC on Shimadzu HPLC system equipped with DGU-20A5R degassing unit, Prominence LC-20AD pumping system, SIL-10AD VP autoinjector, and SPD-10A VP UV/VIS detector (Shimadzu Scientific Instruments, Kyoto, Japan) (Leanpolchareanchai et al. 2014). The integration and system parameters were controlled by LC solution software (Shimadzu Scientific Instruments, Kyoto, Japan). An ACE column (C18; 250 mm × 4.6 mm i.d., particle size 5 µm; Advanced Chromatography Ltd., UK) with a guard column was used as a stationary phase. The elution was performed using gradient solvent systems with a flow rate of 1.2 mL/min at room temperature (25 ± 1 °C). The mobile phase consisted of 0.1% trifluoroacetic acid (Sigma-Aldrich, St. Louis, USA) in DI water (solvent A) and Acetonitrile (ACN, Honeywell, Charlotte, USA) (solvent B). The total run time was 25 min and the gradient program was set as follows: 20% B to 25% B for 3 min, 25% B to 95% B for 2 min, 95% B for 8 min, 95% B to 20% B for 2 min, and 20% B for 10 min, respectively. MSKE and the reference standard, PGG, were dissolved in DI water and methanol, respectively, and the sample injection volume was 10 µL. UV detection was performed by monitoring the absorbance signal at the wavelength of 280 nm. The identification of PGG in MSKE was based on the comparison of the retention time and UV spectrum of the unknown sample peaks with the reference standard, PGG. The retention time of PGG was 4.29 min. The HPLC method was validated for its linearity, precision, accuracy, limit of detection (LOD) and limit of quantitation (LOQ) as per the International Conference on Harmonization (ICH) guidelines. The PGG calibration curve concentration range was 0.2–12.6 µg/mL. The calibration curve linear equation was $y = 22326x - 3779.7$ and the linear correlation coefficient (r^2) was 0.9996. The intra-day and inter-day precision of PGG was evaluated using three concentrations (0.4, 1.5, and 6 µg/mL) and the coefficient of variation was lower than 2%. The method accuracy was determined using a recovery study conducted at three different concentrations (0.4, 1.5, and 6 µg/mL), and the average recovery was 99.89 ± 1.12%. The LOQ and LOD for the PGG chromatographic determination were 0.20 and 0.05 µg/mL, respectively.

2.2.5. Heavy metal residue analysis

Heavy metal residues in MSKE namely, arsenic (As), cadmium (Cd), lead (Pb) and mercury (Hg) were determined according to the Association of Official Analysis Chemists (AOAC) official method of analysis (Latimer 2019). The amounts of As and Hg were determined using flame atomic absorption spectroscopy, while the quantities of Cd and Pb were determined using graphite furnace atomic absorption spectroscopy. The analyses were performed by the National Food Institute (NFI), Bangkok, Thailand.

2.2.6. Pesticide residue analysis

Pesticide residues (organochlorines, organophosphates, pyrethroids, and carbamates) in MSKE were determined using a multi-pesticide residue screening (Lee et al. 1991). The analyses were performed by NFI, Bangkok, Thailand.

2.2.7. Total aflatoxin analysis

Total aflatoxin in MSKE was determined using a fluorometer according to AflaTest® fluorometer instruction manual, developed by VICAM. The analysis was performed by NFI, Bangkok, Thailand.

2.2.8. Moisture content analysis

Moisture content of MSKE was analyzed using a MA50.R moisture analyzer (Radwag, Poland) at a temperature of 105 °C with fully automatic shutoff mode enabled at the end of analysis when a constant weight of sample was obtained (DMSc, 2020). A sample of approximately 400 mg was added to an aluminum pan and distributed evenly before analysis. The moisture content determination was performed in triplicate and expressed as percentage.

2.2.9. Endotoxin assay

An endotoxin assay was performed using Pierce™ LAL Chromogenic Endotoxin Quantitation Kit. All glassware used for collecting MSKE, extracting steps, and LAL assay were sterilized at 120 °C for at least 2 h.

2.3. Molecular modeling

In silico molecular docking calculations using AutoDock Vina (version1.2) (Eberhardt et al. 2021) were employed to analyze molecular mechanisms of main phytochemical compounds including pentagalloyl glucose (PGG), methyl gallate (MG), and gallic acid (GA) within MSKE in comparison with DOX, as the reference for conventional treatments. Crystallographic structures of the target proteins, including epidermal growth factor receptor (EGFR), phosphatidylinositol-4,5-bisphosphate 3-kinase catalytic subunit alpha (PIK3CA), transforming growth factor beta receptor I (TGFβRI), and vascular endothelial growth factor (VEGF) were obtained from Protein data bank (PDB) (Berman et al. 2000; Stamos et al. 2002; Sawyer et al. 2004; Mandelker et al. 2009; Bold et al. 2016). The binding energy score from the best binding mode of each MSKE compound and DOX was estimated and compared to the standard inhibitor found in complex with the target protein, referred as the 'redocking' calculations from crystallographic structural data (Erlotinib (EGFR inhibitor), Wortmannin (PIK3CA inhibitor), LY-580276 (TGFβR1 inhibitor), and AAL993 (VEGF inhibitors)). After the calculations, selected binding complexes with better binding energy scores than the standard inhibitors were visualized by the visual molecular dynamics (VMD) software and Ligplot (Humphrey et al. 1996; Laskowski and Swindells 2011).

2.4. Anticancer activities of MSKE, phytochemical compounds, DOX, and combinations against 2D-HepG2 and 3D-HepG2 spheroid models

2D-HepG2 cells were exposed to MSKE, PGG, GA, MGA, and DOX and were analyzed using the cell proliferation reagent WST-1. In brief, HepG2 cells were routinely seeded at 30,000 cells/well and cultured into each well of a 96-well plate, in completed medium containing Dulbecco's modified eagle medium (DMEM) with 10% fetal bovine serum (FBS) and 1% penicillin-streptomycin antibiotics and maintained at 37 °C with 5% CO_2 incubator. At a confluence, the cells were exposed to MSKE, PGG, GA, MGA, and DOX at concentrations ranging from 0 to 1000 µg/mL (MSKE), 0–200 µg/mL (PGG, GA, and MGA), and 0–100 µg/mL (DOX), respectively, for 24 h. The exposed media were removed and the fresh media with tetrazolium salt of WST-1 (1:10 final dilution following manufacturing protocol) were added to the cells. The cells were then incubated at 37 °C with 5% CO_2 for 15 minutes. After 15 min, the media were collected into the new 96-well plate and measured absorption at the wavelength of 440 nm. The percentage of cell viability was

calculated according to the control of non-treated cells, and data were presented as the percentage of cell viability in proportion to that of the non-treated cells with SD. In addition, 50% inhibitory concentration (IC_{50}) values of MSKE, PGG and DOX were calculated. The different concentrations between either MSKE or PGG with DOX (MSKE-DOX and PGG-DOX) at the same ratio were also investigated for the synergistic effect. The effects of combined treatment were determined using the combination index analysis (CI) following the Chou-Talay method (Chou 2010). The CI will be calculated by CompuSyn software (Version 1.01, ComboSyn, Inc., Paramus, NJ, USA). The results were expressed as CI values, where CI <1, CI =1, and CI >1 indicated synergistic, additive, and antagonistic effects, respectively (Chou 2010; Ediriwickrema et al. 2014). The combined synergistic effects were further assessed the toxicity against 3D-HepG2 models.

For 3D-HepG2 mono and coculture models, the spheroids were exposed to DOX, MSKE and/or PGG at concentrations based on their IC_{50} values obtained from 2D-HepG2 culture model. HepG2 cells were seeded at range 800–1,000 cells/well in 96-ultralow attachment plates to fabricate the 3D-HepG2 monoculture model while, HepG2 cells were seeded at range 800–1,000 cells/well of the 96-ultralow attachment plates with 10% primary HSCs to form the 3D HepG2 coculture spheroids and maintained at 37 °C with 5% CO_2 according to our previous work (Sae-be et al. 2023). At day 10 after seeding, the 3D HepG2 spheroids were exposed to DOX, MSKE and the combined MSKE-DOX at concentrations 1, 2, 5, and 10 times of their IC_{50} obtained from 2D-HepG2 cells for 24 h at 37 °C with 5% CO_2. After incubation, 3D-HepG2 spheroids were, then, rinsed with Dulbecco's phosphate buffer saline (DPBS) and further incubated with the medium containing WST-1 for 3 h in 3D-HepG2 spheroids. The medium was collected and measured the absorbance at the wavelength of 440 nm. The percentage of cell viability was calculated according to the control of non-treated cells, and data were presented as the percentage of cell viability in proportion to that of the non-treated cells with SD. The different ratios of MSKE-DOX were also investigated. The percentage of cell viability was calculated as mentioned above. Experiments were performed in triplicate ($n = 3$).

2.5. Anticancer activity of MSKE against 3D-imHC spheroids

Immortalized hepatocyte-like cells (imHCs) were developed by transfecting human mesenchymal stem cells with hTERT plus Bmi-1 (Sa-Ngiamsuntorn et al. 2011) and the cells were routinely characterized using our previously published protocol. imHC cells were routinely cultured in completed DMEM. At confluence more than 90%, imHC cells were seeded at range 800–1,000 cells/well of an ultralow attachment 96-well plate with 10%HSCs to form imHC coculture spheroids according to our previous work (Sae-be et al. 2023). The media were changed every 3–4 days after seeding. At day 10 after seeding, the 3D imHC spheroids were exposed to MSKE at concentrations ranging 0–1,200 µg/mL for 24 h. Viability of 3D-imHC spheroids was evaluated after exposing to MSKE for 24 h, using WST-1 assay as described above (in section 2.4). The percentage of cell viability was calculated according to the control of non-treated cells, and data were presented as the percentage of cell viability in proportion to that of the non-treated cells with SD. The experiments were done in triplicate ($n = 3$).

2.6. HMSN synthesis, characterization and drug encapsulation

2.6.1. Preparation of HMSNs, NH_2HMSNs, and GQD-NH_2HMSNs

HMSNs were synthesized by a hard-template method using dense silica nanoparticles ($dSiO_2$ NPs) as cores before modifying surface and etching process (Wu et al. 2013). Firstly, $dSiO_2$ NPs were synthesized by the modified StÖber method (Greasley et al. 2016). In brief, 20 mL absolute ethanol was mixed with 7 M of DI water and 0.11 M of 28%–30% ammonium hydroxide (NH_4OH,). Then, the mixed solution was stirred for 10 min before adding 0.28 M of tetraethyl orthosilicate (TEOS) to react at room temperature (25 ± 1 °C) overnight. Afterward, $dSiO_2$ NPs, 10 mL, were washed and resuspended in DI water. Secondly, $dSiO_2$ NPs were modified the surface to form mesoporous character. Cetyltrimethylammonium chloride solution (CTAC, 2 g) and triethylamine (TEA, 20 mg) were dissolved in 20 mL of DI water and stirred for 1 h before adding the 10 mL of resuspended $dSiO_2$ NPs. TEOS, 0.15 mL, was dropwise added into the mixture. The reaction took place at 80 °C for 1 h with vigorous stirring at 400 rpm. The etching process involved solubilizing the cores with Na_2CO_3 solution (Chen et al. 2014; Kong et al. 2017). The mixture was

cooled down to 50 °C before adding 500–850 mg of Na_2CO_3 under vigorous stirring for 30–45 min to form the hollow structure. CTAC in HMSNs was removed by ultrasonic extraction using acidic ethanol (37% (w/w) hydrochloric acid (HCl): absolute ethanol, 4:100 v/v) for 5 cycles at 12,000 rpm for 20 min, each, and then, dried under vacuum (Kong et al. 2017; Liu et al. 2019). Amino group (NH_2) modification at surfaces of HMSNs (NH_2HMSNs) was carried out by dispersing 40 mg of HMSNs in 20 mL of toluene, followed by the addition of 1 mL of (3-aminopropyl) triethoxysilane (APTES). The system was kept and stirred at 80 °C with N_2 atmosphere for 24 h. The suspension of NH_2HMSNs was centrifuged at 12,000 rpm for 15 min and rinsed by ethanol at least 3 times to remove toluene (Liu et al. 2016; Ezzati et al. 2019). NH_2HMSNs were further employed to load MSKE before capping by GQDs. To fabricate GQD-NH_2HMSNs, 5 mL of GQDs (1 mg/mL) were activated by 10 mg/mL of 1-ethyl-3-(3-dimethylaminopropyl) carbodiimide hydrochloride (EDC) and 5 mg/mL of N-hydroxysuccinimide (NHS) for 4 h at room temperature (25 ± 1 °C). Subsequently, 20 mg of NH_2HMSNs resuspended in 1 mL of DI water, was slowly added into the activated GQDs solution and the reaction mixture was stirred for 24 h in a dark condition at 4 °C. GQD-NH_2HMSNs were collected by centrifugation at 12,000 rpm for 15 min and then washed with DI water at least 3 times to remove the residual EDC, NHS, and GQDs before drying in a vacuum (Yao et al. 2017). The synthesized NPs were characterized for particle size, particle size distribution (TEM, NanoZiser ZS) and surface charge density (NanoZiser ZS). Chemical structures of NPs and the remaining CTAC and toluene were observed using FTIR.

2.6.2. Preparation of DOX-HMSNs and GQD-MSKE-NH_2HMSNs

HMSNs, 20 mg, incubated with DOX solution (0.5 mg/mL in PBS, 12 mL) for 24 to prepare DOX-HMSNs. While 20 mg of NH_2HMSNs was incubated with MSKE solution (0.5 mg/mL in PBS, 20 mL) at room temperature (25 ± 1 °C) for 24 h. Then, the mixtures were stirred for 24 h at 600 rpm. The suspensions of DOX-HMSNs and MSKE-NH_2HMSNs were centrifuged at 12,000 rpm for 15 min and washed by DI water to remove the unbound DOX and unbound MSKE. The supernatants were collected and measured the concentrations of DOX at the wavelength of 480 nm to calculate the % encapsulation efficiency (%EE) and % loading capacity (%LC) following the Eqs. (1) and (2), respectively (Zhang et al. 2014). DOX-HMSNs were dried in a vacuum at room temperature (25 ± 1 °C). The dry powder of DOX-HMSNs was obtained and further used for the next experiments.

$$\%EE = (\text{Weight of drug in nano carriers} / \text{Initial weight of drug}) \times 100 \quad (1)$$

$$\%LC = (\text{Weight of drug in nano carriers} / \text{Weight of drug} - \text{loaded nano carriers}) \times 100 \quad (2)$$

The amount of PGG in the supernatants (analyzed by HPLC) was used as a phytochemical marker to calculate the concentration of MSKE. %EE and %LC of MSKE in NH_2HMSNs were determined following the Eqs. (1) and (2) above. MSKE-NH_2HMSNs were further capped with GQDs at the surface using the same protocol to fabricate GQD-NH_2HMSNs (as previously described in the synthesis section).

2.6.3. Hydrodynamic diameter (HD), size distribution, and zeta potential analysis

The hydrodynamic diameter (Z-average) and polydispersity index (PDI) of the resuspended $dSiO_2$ NPs, HMSNs, DOX-HMSNs, and GQD-MSKE-NH_2HMSNs (10 µg/mL in DI water) were measured by dynamic light scattering (DLS) using a Zetasizer Nano (Malvern, UK). The resuspended HMSNs, NH_2HMSNs, GQD-NH_2HMSNs, DOX-HMSNs, MSKE-NH_2HMSNs, and GQD-MSKE-NH_2HMSNs (10 µg/mL in DI water) were measured zeta potential using the Zetasizer Nano (Malvern, UK). The experiments were conducted in triplicate ($n = 3$) with 10 readouts on each experiment.

2.6.4. Surface area, pore volume, and pore size analysis

The N_2 adsorption/desorption isotherms were obtained using Autosorb iQ-MP (Anton Paar, Austria). BET (Brunauer-EmmettTeller) multipoint analysis was used to calculate the specific surface area. The pore volume and distribution measurements were obtained using Barrett-Joyner-Halenda (BJH) methods (Pinna et al. 2021). The samples were prepared by degassing at 200 °C for 24 h at 10 °C/min before the analysis.

2.6.5. TEM analysis

Samples for size and morphology analysis using transmission electron microscopy (TEM) were prepared by applying the suspension of NPs on lacey carbon-coated copper TEM grids, 200 mesh, placed over parafilm on filter paper. The samples were diluted to one-tenth of the original concentration by combining 30 µL of NP suspension with 270 µL of absolute ethanol for $dSiO_2$ NPs and HMSNs and DI water for GQDs, GQD-NH_2HMSNs, DOX-HMSNs, and GQD-MSKE-NH_2HMSNs. The samples were mixed well, and then 10 µL of NP suspension was pipetted onto the grids. Grids were left to deposit for 20 min before excess samples were absorbed by the filter paper. Samples were kept in a desiccator before viewing. The sample grids were observed using JEOL 2010 transmission electron microscope (JEM-2010, JEOL, Japan) operated at an accelerating voltage of 200 kV using magnification 10K–500K to examine the morphology and size. High resolution TEM (HR-TEM) was performed on an image-corrected JEOL 2010 TEM operated at 200 kV using magnification 600K to examine the morphology of GQDs using selected area electron diffraction (SAED) pattern mode.

2.6.6. Fourier transform-infrared spectroscopy (FT-IR)

The functional groups of DOX, MSKE and all designed NPs (powder form) were elucidated using an attenuated total reflection (ATR) for FT-IR spectroscopy. Samples of NPs, DOX, and MSKE were recorded using Nicolet iS5 FT-IR Spectrometer (Thermo Fisher Inc., Massachusetts, USA). The measurement was conducted in the range of 4000–400 cm^{-1} at a resolution of 4 cm^{-1}.

2.7. Photothermal property of GQD-MSKE-NH_2HMSNs

To measure the photothermal property of GQD-MSKE-NH_2HMSNs, different concentrations (0.1, 0.25, 0.5, and 1.0 mg/mL) of GQD-MSKE-NH_2HMSNs suspension, 200 µL, in the 96-well plate were exposed to a 785 nm laser (Changchun New Industries Optoelectronics Technology, Changchun, China) at 3.0 W/cm^2 for 10 min. While GQD-MSKE-NH_2HMSNs suspension at 0.5 mg/mL was irradiated by different power intensities (0.5, 1.0, 2.0, and 3.0 W/cm^2). A thermometer using a NIR camera (InfiRay (C200Pro), Yantai, China) was employed to measure the temperature profiles during irradiation. Furthermore, the photostability of GQD-MSKE-NH_2HMSNs, 0.5 mg/mL, was detected using on-off cycles (5 cycles) at 785 nm NIR laser with 3.0 W/cm^2 (Chen et al. 2014; Yao et al. 2017).

2.8. Drug release study

In vitro drug release study of DOX-HMSNs was performed *via* centrifugation method in PBS at pH 5.0 and pH 7.4 (Kong et al. 2017). Briefly, 2.0 mg of DOX-HMSNs was suspended in 1 mL PBS medium before placing in the shaking incubator (ThermoMixer®C, Eppendorf, Germany) with a shaking speed of 1,000 rpm at 37 °C. At time (T) = 0, 2, 4, 6, 8, 18, 20, 24, and 48 h, the sample tubes were collected and centrifuged at 12,000 rpm for 20 min. The supernatants, 800 µL, were collected and quantified the release of DOX using a UV-VIS spectrophotometer (Tecan, Switzerland). The collected volume of medium, 800 µL, was replaced by the fresh medium, and the sample tubes were placed back into the shaking incubator for the release profile study for 48 h. The amount of the released DOX in the supernatants was measured using a UV-VIS spectrophotometer (Tecan, Switzerland) at a wavelength of 480 nm. The calibration curve linear equations at pH 7.4 were, $y = 0.0009x + 0.0248$ with r^2 of 0.9999, and at pH 5.0, $y = 0.0107x + 0.045$ with r^2 of 0.9996, respectively.

Meanwhile, *in vitro* drug release of GQD-MSKE-NH_2HMSNs was performed at 50 °C at the same pH conditions and time points between 0 and 48 h. GQD-MSKE-NH_2HMSNs, 3.0 mg, were dispersed with 1 mL PBS medium and put in a shaking incubator with the shaking speed at 1,000 rpm at 50 °C for 48 h. The supernatants, 800 µL, were filtered through the membrane filter, and the filtrates were assayed using HPLC. The quantity of MSKE was calculated from the content analysis of PGG using HPLC (Leanpolchareanchai et al. 2014; Jiamboonsri et al. 2015).

2.9. Collagen depleting in 3D-HepG2 spheroids by GQD-MSKE-NH_2HMSNs

3D-HepG2 spheroids were exposed to GQD-MSKE-NH_2HMSNs (0.5 mg/mL) in medium and incubated for 6 h. Consequently, the 3D-HepG2 spheroids were irradiated by NIR laser, at 785 nm with 3.0 W/cm^2, for 10 min. The irradiated spheroids were incubated at 37 °C and 5% CO_2 for 15 min, 30 min and 1 h before fixing with 4% paraformaldehyde. The fixed spheroids were permeabilized and blocked with 0.1% Triton-X100 in PBS and with 1% Bovine serum albumin (BSA) and 10% FBS in PBS for 1 h at 25 °C, respectively. Next, the 3D-HepG2 spheroids were incubated with rabbit anti-collagen type I (COL1) antibody (AB34710) at dilution 1:200 overnight at 2–8 °C in the refrigerator. The samples were, then, rinsed several times with PBS before incubating with a secondary donkey anti-rabbit antibody with Alexa Fluor 647 (1:500) for 2 h. Finally, the samples were rinsed and mounted with a mounting medium. The 3D samples were visualized using High Content Screening (HCS) System, Opera Phenix™ Plus (Revvity, Massachusetts, USA). Images were taken with laser power of 100% and exposure time of 800 ms. The stack images were analyzed using Harmony software (version 5.0). The background fluorescence of non-treated cells and non-stained samples were used to optimize the range of fluorescent intensity in image analysis. Mean fluorescent intensity (MFI) of COL1 per area (μm^2) was calculated.

2.10. Cellular uptake of NPs

In brief, 2D-HepG2 cells were routinely seeded at 30,000 cells/well in 96-well plates. At the confluence, 2D-HepG2 cells were incubated with GQD-MSKE-NH_2HMSNs (0.1 mg/mL) in culture medium for 6 and 24 h. Following treatment, the 2D-HepG2 cells were stained with acridine orange (AO) that accumulates in lysosomes due to their acidic environment for 15–30 min. For the 3D model, HepG2 spheroids were treated with GQD-MSKE-NH_2HMSNs (0.1 mg/mL) in culture medium on day 10 after seeding and incubated for 6 and 24 h before AO staining for 30–45 min and viewing. In PTT treatment group, after the GQD-MSKE-NH_2HMSN exposure, 3D-HepG2 spheroids were irradiated by NIR laser at the wavelength of 785 nm with 3.0 W/cm^2 for 10 min. Post irradiation, the 3D-HepG2 spheroids were stained with AO as mentioned above. For visualization, after AO staining both 2D-HepG2 and 3D-HepG2 models were washed several times with PBS and the fresh pre-warmed media were added. The samples were visualized using HCS System, Opera Phenix™ Plus (Revvity, Massachusetts, USA). The stack images were analyzed using Harmony software (version 5.0). Mean fluorescence intensity (MFI) per area (μm^2) of GQD-MSKE-NH_2HMSNs in each group was calculated by Harmony software (version 5.0). Fluorescence from non-treated cells (control; T = 0 h) was quantified and applied as a baseline to subtract background intensity during image analysis.

2.11. Anticancer activity of DOX-HMSNs, GQD-MSKE-NH_2HMSNs, and SNP against 2D-HepG2 cells and 3D-HepG2 spheroids

Cell density to fabricate 2D and 3D-HepG2 models following methods in 2.4 anticancer activity of MSKE, phytochemical compounds, DOX and combinations against 2D-HepG2 and 3D-HepG2 spheroid models. The viability of 2D-HepG2 cells and 3D-HepG2 spheroids was assessed following each treatment including DOX-HMSN treatment group, GQD-MSKE-NH_2HMSN treatment group, and the SNP treatment group (triple combination therapy) using WST-1 assay. The SNP treatment consists of 3 steps: (i) exposure to GQD-MSKE-NH_2HMSNs, (ii) the NIR laser irradiation at the wavelength of 785 nm, and (iii) exposure to DOX-HMSNs, respectively.

For the 2D model, at confluence, the cells were divided into 3 groups and treated as mentioned above. In the SNP treatment group, cells were first incubated with GQD-MSKE-NH_2HMSNs for 6 hours, followed by NIR laser irradiation at 785 nm (3.0 W/cm^2) for 10 min. After irradiation, cells were incubated for an additional hour before exposure to DOX-HMSNs. The exposed concentrations of MSKE and DOX were ranged from 1/8 $IC_{50(2DHepG2)}$ to 1 $IC_{50(2DHepG2)}$ of each compound based on non-encapsulated drugs, and in SNP treatment group the same concentration ranges of MSKE and DOX were applied. Following 24-hour incubation period with DOX-HMSNs, both 2D models were rinsed with DPBS and incubated with

the medium containing WST-1 for 15 min (2D-HepG2 model). The medium was collected and measured the absorbance at the wavelength of 440 nm.

For the 3D models, after day 10 the spheroids were divided into 3 groups and treated as mentioned above. The exposed concentrations of MSKE and DOX were ranged from 1/8 $IC_{50(3DHepG2)}$ to 1 $IC_{50(3DHepG2)}$ of each compound based on non-encapsulated drugs, and in SNP treatment group the same concentration ranges of MSKE and DOX were applied. Following 24-hour incubation period with DOX-HMSNs, 3D-HepG2 models were rinsed and incubated with the medium containing WST-1 for 3 h. Then the medium was collected and measured the absorbance at the wavelength of 440 nm. In addition, the effect on spheroid size (diameter, µm) in each treatment group was measured based on the outmost edge of each tumor spheroid and calculated as the square root of two orthogonal diameters: the longest axis (d1) and the shortest axis (d2) ($D = \sqrt{d1d2}$) (Shi et al. 2018).

All experiments were performed in triplicate ($n = 3$). The anticancer efficacy of each treatment was evaluated by comparing cell viability to that of the single-agent treatments and the combination of non-encapsulated MSKE and DOX.

2.12. Cell death mechanism

2.12.1. Lactate dehydrogenase (LDH) assay

The extent of cell membrane damage caused by DOX, MSKE, GQD-MSKE-NH_2HMSNs, DOX-HMSNs, and SNP, was evaluated using the LDH assay for 24 h exposure period according to the manufacturer's instructions. 2D-HepG2 cells were seeded at a density of 30,000 cells/well in 96-well plates and cultured until reaching confluence. The cells were then treated with DOX, MSKE, GQD-MSKE-NH_2HMSNs, DOX-HMSNs, and the SNP formulation at their IC_{50} concentrations for 24 h. Subsequently, 50 µL of cell-free medium from each group was mixed with 50 µL of freshly prepared LDH mixture (containing the LDH substrate and assay buffer) in a 96 well plate. The control and positive control groups were cells without any treatment and cells with the addition of lysis buffer (indicating maximum LDH release), respectively. Another control group was unloaded NPs that were used to confirm the noninterference of the NPs with the assay. The plate was incubated in the dark for 30 min, and the absorbance was recorded at 490 nm. Data were calculated according to LDH manufacturing protocol.

2.12.2. In vitro cell apoptosis assay

2D-HepG2 cells were seeded at a density of 30,000 cells/well in 96-well plates and cultured until reaching confluence. For 3D spheroids cells were seeded as mentioned in Section 2.4. The cells were then treated with DOX, MSKE, GQD-MSKE-NH_2HMSNs, DOX-HMSNs, and the SNP formulation at their IC_{50} concentrations for 24 h. Untreated cells served as the control group. Following treatment, cells were harvested and washed with DPBS, then resuspended in Annexin V binding buffer before staining by Annexin V-FITC (Excitation/Emission: 499 nm/518 nm) and propidium iodide (PI, Excitation/Emission: 535 nm/617 nm) for 15 minutes in the dark at room temperature. The cells were stained with PI (seeing in red at nuclei as PI intercalation with the DNA) and annexin V (seeing green at cell membrane as annexin V selectively bind to phosphatidylserine on the cell membrane). Viable cells were identified as those negative stained of both Annexin V-FITC and PI. To identify the three stages of cell death, early apoptosis, late apoptosis, and necrosis, we quantified number of cells observed in green at cell membrane (as early apoptosis), red at nuclei together with green at the cell membrane of the same cell (as late apoptosis), and red at the nuclei (as necrosis), respectively. The stained cells were then imaged using a High Content Screening (HCS) System, Opera Phenix™ Plus and analyzed by Harmony software (version 5.0) (Revvity, Massachusetts, USA).

2.13. Statistical analysis

Data were presented as the mean ± standard deviation (SD) where three independent experiments were performed. The data will be first tested by Shapiro-Wilk normality test ($\alpha = 0.05$, $p > 0.05$) to confirm a normal distribution (Graph Pad Prism version 10.0). The difference in the collagen depletion assay, anticancer activity assay of non-encapsulated drugs, the single platform (DOX-HMSNs or GQD-MSKE-NH_2HMSNs) and

the SNP groups at different concentrations, and LDH assay were analyzed using one-way ANOVA with a post-hoc (Tukey's) test to confirm differences. Significant differences in drug release conditions, size alteration of spheroids were determined using two-way ANOVA with a post-hoc, Bonferroni. The difference in cell death mechanism was determined using two-way ANOVA with a post-hoc, Tukey's. The letters a and b were used to represent significant difference within treatment groups (early apoptosis (as control), late apoptosis and necrosis) and between treatment groups (non-treated groups as control), respectively. All statistical analysis will be performed using Graph Pad Prism version 10.0. Differences will be considered significant at $^{*}p \leq 0.05$, $^{**}p \leq 0.01$, $^{***}p \leq 0.001$, and $^{****}p \leq 0.0001$, $n = 3$.

3. Results and discussion

3.1. Mango seed kernel extraction, phytochemical studies and quality controls

MSKE extracted by the decoction method using 95% v/v ethanol and dried by the freeze-drying method was observed in light-brown powder with % yield of 9.36%. Total phenolic and total flavonoid contents of MSKE were 57.36 ± 1.38%g equivalent to gallic acid (GA)/100 g MSKE and 3.48 ± 0.91%g equivalent to quercetin (QE)/100 g MSKE, respectively. The results were consistent with the previous studies, in which the phenolic compounds were major compounds in MSKE (Mirza et al. 2021). In addition, the freeze-drying method could retain phenolic compounds due to a lack of heat-related damage (Sogi et al. 2013). All impurity residues in MSKE met the requirements according to the Thai Herbal Pharmacopeia 2020 (DMSc 2020). The contents of arsenic (As), cadmium (Cd) and mercury (Hg) were not detected at the detection limits of 0.010, 0.010, and 0.007 ppm, respectively, while the content of lead (Pb) was less than the quantitative limit (<0.03 ppm). The pesticide residues and total aflatoxin were not detected in MSKE. Moisture content is an important factor in determining the stability of powder storage. The percentage of moisture content of MSKE was 4.86 ± 0.14% which aligned with the recommendation of Thai Herbal Pharmacopeia 2020, where the herbal product should contain less than 10% of moisture content to prevent product instability and microbial contamination (DMSc 2020). The endotoxin level was found to be between 0.0590 ± 0.006EU/mL, indicating low level endotoxin contained in MSKE.

The phytochemical profiles of compounds in MSKE were different depending on region of cultivation, extraction method and drying process. Several reports revealed that the phenolic compounds in MSKE consisted of GA, chlorogenic acid, caffeic acid, MGA, and gallotannins (Jiamboonsri et al. 2015; Shaban et al. 2023). Previous studies revealed the main phenolic compounds in MSKE obtained from *M. indica* cv. 'Fahlun' were PGG (61.28% w/w), MGA (0.68% w/w), and GA (0.44% w/w), respectively, using high performance-thin layer chromatography (HP-TLC) (Nithitanakool et al. 2009). PGG was the highest yield in MSKE; therefore, the PGG was selected as a phytochemical marker to calculate the amount of MSKE (Nithitanakool et al. 2009; Leanpolchareanchai et al. 2014; Jiamboonsri et al. 2015). Both HP-TLC and HPLC are employed to identify and quantify the main constituents within herbal extracts. However, HPLC provides more accurate data than HP-TLC for quantitative analysis (Leanpolchareanchai et al. 2014; Loescher et al. 2014; Jiamboonsri et al. 2015), and the HP-TLC analysis could not separate between penta-O-galloyl-glucoside and other galloyltannins (hexa-, hepta-, octa, and nona-O-galloyl-glucoside) resulting in a high estimation of PGG (61.28%w/w) (Luo et al. 2014). Therefore, PGG in MSKE was quantified using HPLC. The concentration of PGG in MSKE was 9.26 ± 0.96% w/w which corresponds to results from our previous studies, 9.24 ± 0.96% w/w (Leanpolchareanchai et al. 2014; Jiamboonsri et al. 2015). The chromatogram of PGG, compared to standard PGG was showed in Figure S1.

Pharmacological activities of MSKE including anti-cancer and cancer prevention may relate to phenolic compounds (Nithitanakool et al. 2009; Mirza et al. 2021; Shaban et al. 2023). MSKE exhibited strong antiproliferative activity against HepG2 ranging from 33.91 to 41.50 µg/mL depending on cultivars of *M. indica* L (Luo et al. 2014). PGG (Dong et al. 2014; Kant et al. 2016; 2019; Jiang et al. 2023), MGA (Huang et al. 2021; Liang et al. 2022), and GA (Lima et al. 2016; Shi et al. 2021) have been reported for HCC treatment *via* several mechanisms both *in vitro* and *in vivo*. PGG exerted its anticancer activity against liver cancer cells by autophagy-mediated senescence, arresting cells in G1 and S phases and inducing apoptosis (Dong et al. 2014; Jiang et al. 2023). PGG also inhibited the growth of Huh7 xenograft mice *via* the upregulation of a tumor suppressor, glycine N-methyltransferase (GNMT) through the inhibition

of MYC mRNA expression (Kant et al. 2016; 2019). MGA induced apoptosis of HCC cells by increasing levels of intracellular oxidation and superoxide production (Huang et al. 2021). Furthermore, MGA had anti-proliferation against HCC cells through downregulation of adenosine monophosphate-activated protein kinase (AMPK)/nuclear factor-κB (NF-κB), which is a pathway to control tumor migration, invasion and angiogenesis. *In vivo* HCC xenograft models demonstrated the reduction of matrix metalloproteinases (MMP) 9 and MMP2 which are proteins to promote epithelial-mesenchymal transition (EMT) in the MGA treatment group (Liang et al. 2022). Therefore, MGA could prevent HCC metastasis. While GA had anti-proliferative and pro-apoptotic effects in HepG2 cells without interfering with the cell cycle, it also suppressed tumorigenesis through the Wnt/β catenin pathway (Shi et al. 2021). Nevertheless, molecular mechanisms against target proteins overexpressing in HCC of these phenolic compounds have not been studied.

3.2. Molecular modeling

Molecular docking calculations were performed to investigate binding affinities of the phytochemical compounds in MSKE (PGG, MGA, and GA) and DOX against target HCC proteins (Table 1). Epidermal growth factor receptor (EGFR), phosphatidylinositol-4,5-bisphosphate 3-kinase catalytic subunit alpha (PIK3CA), transforming growth factor beta receptor 1 (TGFβR1) and vascular endothelial growth factor (VEGF)-targeted therapy of HCC, were selected in this study (Xia et al. 2018; Llovet et al. 2021). The targeted therapy such as EGFR inhibitors and VEGF inhibitors has been approved for HCC treatment with single and combination therapy (EASL, 2018; Llovet et al. 2021). Table 1 presented the estimated binding energy scores of all compounds and the binding conformations with target proteins in Figure 1. According to the docking calculation (kcal/mol) results, PGG interacted with all target HCC proteins with significantly lower energy than MGA and GA, which represented a strong binding of the PGG. This might be due to the relatively large surface area of PGG. Compared to DOX, PGG could bind to PIK3CA and TGFβR1 with stronger binding energy of −9.2 and −9.7 kcal/mol, respectively. In contrast, the binding between PGG with EGFR (−9.8 kcal/mol) was slightly weaker than DOX (−10.5 kcal/mol). However, the binding between PGG and EGFR was significantly stronger than that of the drug inhibitor, Erlotinib (−7.5 kcal/mol). The binding of PGG spanned over a greater number of amino acid residues in the pocket of EGFR due to its star-shaped geometry, in which each tip contained the chemical structure of a gallic acid with hydrogen bonds forming hydroxyl groups. Meanwhile, the binding between PGG and VEGF (−6.6 kcal/mol) indicated that the interactions were significantly weaker than its known inhibitor, AAL993, (−12.0 kcal/mol) and DOX (−8.1 kcal/mol), respectively.

Figure 1 displayed the best binding modes of the compounds to the target proteins—EGFR (Figure 1A), PIK3CA (Figure 1B), TGFβR1 (Figure 1C), and VEGF (Figure 1D)—as the results of molecular docking calculations. The complexes of all protein targets demonstrated some common trends, as GA and MGA compounds (in blue and cyan, respectively) with smaller sizes were found within the deeper parts of binding pockets, especially for VEGF with a narrow and deep pocket. Meanwhile, DOX and PGG (in pink and green, respectively) with relatively larger sizes tended to bind with the pocket entrances. To elucidate the molecular interactions between target proteins and compounds from MSKE in comparison to the inhibitors and DOX, Figure 2(A–D) provided the mapping between hydrogen bonds and hydrophobic contacts found between amino acid residues and the best binding modes of the compounds.

The EGFR protein was found in complex with the reference inhibitor 'erlotinib' mainly through hydrophobic contacts, while DOX and PGG interacted with less numbers of hydrophobic contacts but with 2–4 additional hydrogen bonds. Meanwhile, GA and MGA were bound with EGFR at partly

Table 1. *In silico* results of calculated binding energy scores (kcal/mol) between therapeutic agents and target proteins overexpressing in HCC.

Protein targets	Inhibitor	Redocking (kcal/mol)	DOX (kcal/mol)	PGG (kcal/mol)	MGA (kcal/mol)	GA (kcal/mol)
EGFR	Erlotinib	−7.5	−10.5	−9.8	−5.7	−5.9
PIK3CA	Wortmannin	−9.0	−8.5	−9.2	−5.8	−5.7
TGFβR1	LY-580276	−10.8	−8.5	−9.7	−6.8	−7.0
VEGF	AAL993	−12.0	−8.1	−6.6	−6.2	−6.1

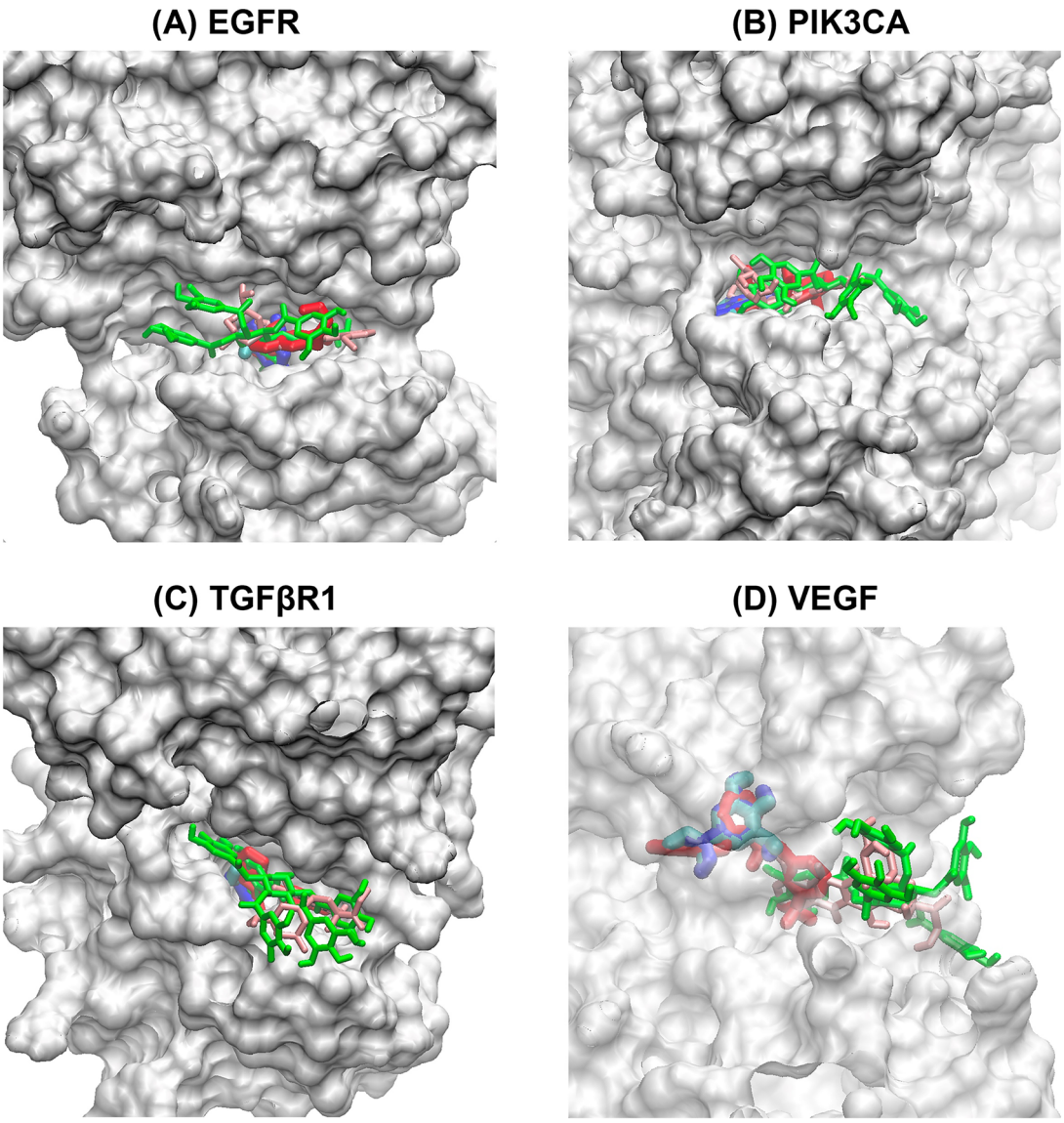

Figure 1. Molecular docking between active compounds in MSKE and the target HCC proteins: Binding conformations of the best docking modes of DOX (pink), GA (blue), MGA (cyan), PGG (green), and the reference inhibitors (red) from PDB structures on the EGFR (A), PIK3CA (B), TGFβR1 (C), and VEGF (D).

similar amino acid residues to DOX and PGG (Figure 2A). Figure 2(B) displayed a similar trend of PIK3CA to EGFR with shallow binding pockets that DOX and all MSKE compounds shared some binding residues while adding up several hydrogen bonds to the interaction network from the relatively hydrophobic wortmannin as the reference inhibitor. The trend of hydrogen bonding of DOX and MSKE compounds was still observed for the TGFβR1 protein (Figure 2C) while the reference inhibitor, LY-580276, mostly contains aromatic rings interacted at the ATP-binding site of TGFβR1 *via* the creation of up to 13 hydrophobic contacts. However, the difference in hydrophobic binding contacts was now observed between DOX and MSKE compounds as there was only one common binding residue between GA/MGA and PGG. GA and MGA formed interaction networks at unique sites located deep into the TGFβR1 binding pocket (Figure 1C). Similarly, Figure 2(D) showed that GA and MGA formed unique interaction networks with VEGF as they were located deep within the narrow binding pocket (Figure 1D). Meanwhile, DOX and PGG displayed more common binding sites to VEGF protein (Figure 2D). Therefore, GA, MGA, and PGG were further investigated for their anticancer activities against HepG2 models.

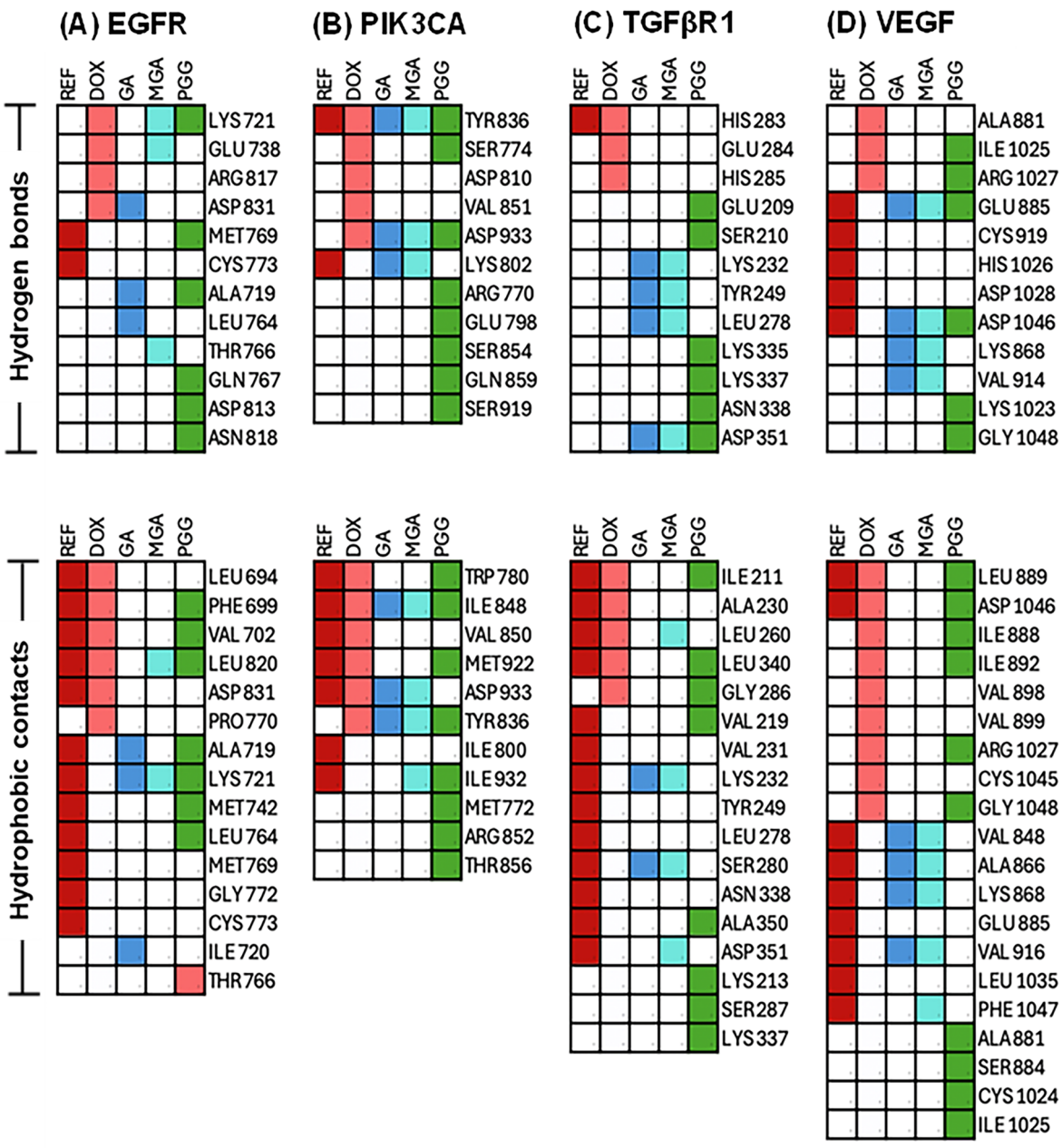

Figure 2. Interaction maps of active compounds in MSKE and the amino acid residues of the target HCC proteins: the amino acid residues of the EGFR (A), PIK3CA (B), TGFβR1 (C), and VEGF (D) targets formed hydrogen bonds (top) and hydrophobic contacts (bottom) with DOX (pink), GA (blue), MGA (cyan), PGG (green), and the reference inhibitors (REF; red).

3.3. Anticancer activities of MSKE, phytochemical compounds in MSKE, DOX, and combinations against 2D-HepG2 cells and 3D-HepG2 spheroids

Following the *in-silico* study, anti-cancer activities of phytochemical compounds against 2D-HepG2 cells following 24 h exposure period were investigated and compared to MSKE. The $IC_{50(2D\text{-}HepG2)}$ values of MSKE against 2D-HepG2 cells were 218.48 ± 9.81 µg/mL, respectively (Figure 3A). While $IC_{50(2D\text{-}HepG2)}$ of PGG, GA, and MGA were 42.13 ± 3.14 µg/mL, 190.1 ± 1.06, and 179.5 ± 1.42, respectively (Figure 3B). Therefore, PGG had the highest anticancer activity and exhibited significantly higher anticancer activity than MSKE. In addition, PGG could inhibit the proliferation of other subtypes of HCC cells including Huh7, Hep3B, SK-HEP-1, and Mahlavu in a dose-dependent manner and also be used as an adjuvant therapy with sorafenib to provide synergistic effects against HCC (Kant et al. 2016). Thus, PGG was

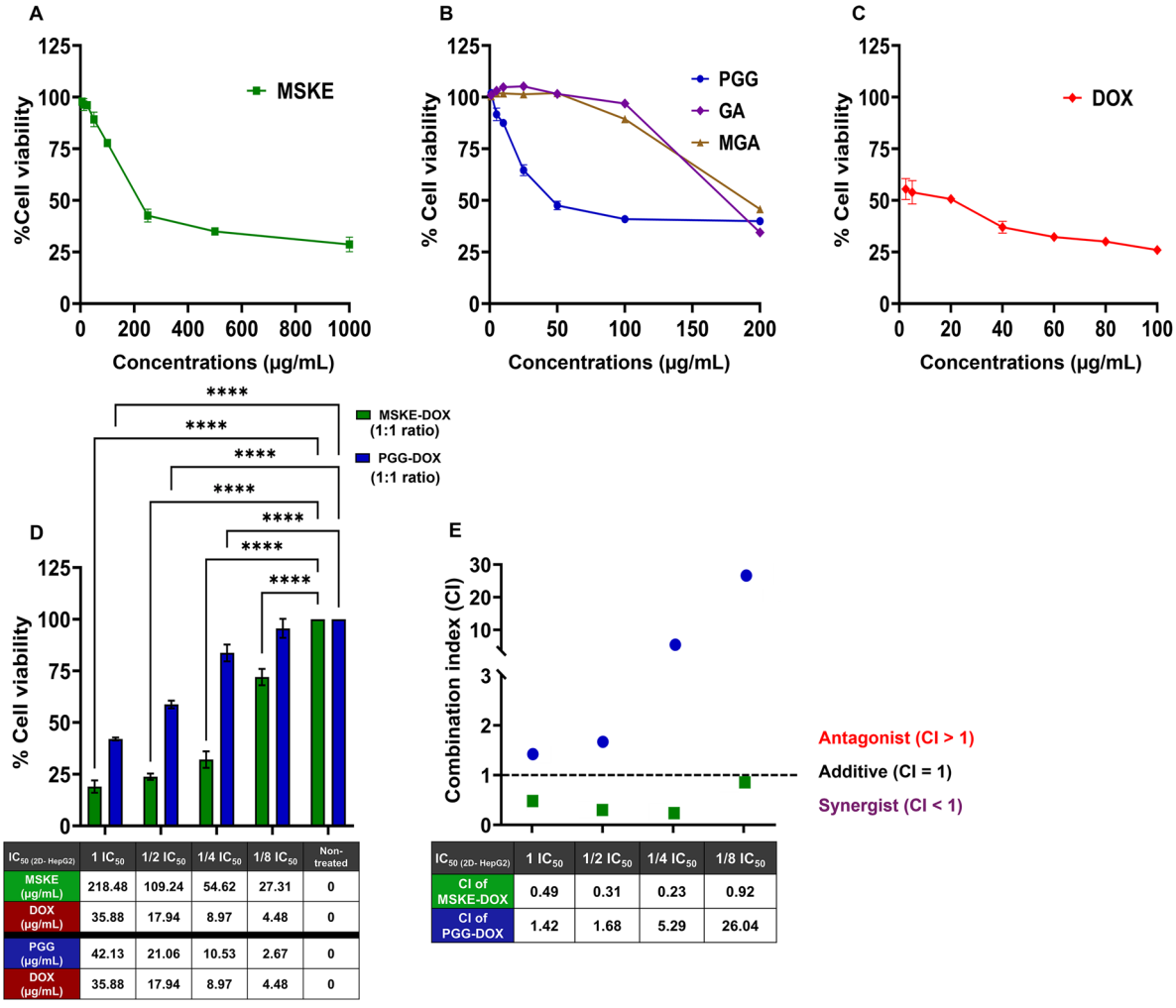

$IC_{50\ (2D\text{-}HepG2)}$	1 IC_{50}	1/2 IC_{50}	1/4 IC_{50}	1/8 IC_{50}	Non-treated
MSKE (µg/mL)	218.48	109.24	54.62	27.31	0
DOX (µg/mL)	35.88	17.94	8.97	4.48	0
PGG (µg/mL)	42.13	21.06	10.53	2.67	0
DOX (µg/mL)	35.88	17.94	8.97	4.48	0

$IC_{50\ (2D\text{-}HepG2)}$	1 IC_{50}	1/2 IC_{50}	1/4 IC_{50}	1/8 IC_{50}
CI of MSKE-DOX	0.49	0.31	0.23	0.92
CI of PGG-DOX	1.42	1.68	5.29	26.04

Figure 3. Anticancer activity of each active compound in MSKE and combinations in 2D model: % cell viability of MSKE(A), PGG, GA and MGA (B) and DOX (C) against 2D-HepG2 cells following 24 h exposure periods. % cell viability (D) and the combination index (CI) of the combination therapy (E) including MSKE-DOX and PGG-DOX against 2D-HepG2 cells at 1 IC_{50} to 1/8 IC_{50} ($n = 3$, mean ± SD).

selected to co-delivery with DOX and further tested in 3D-HepG2 models. The $IC_{50(2D\text{-}HepG2)}$ of DOX against HepG2 cells was 35.88 ± 1.67 µg/mL (Figure 3C). This is the first time that the anticancer activities of the combined MSKE-DOX and PGG-DOX were examined and compared their synergistic effects against HCC. The combination index (CI) of each treatment was calculated following Chou-Talalay method using CompuSyn software (Version 1.01) (Chou 2010; Ediriwickrema et al. 2014). Fascinatingly, the co-exposure of MSKE-DOX at different concentrations (2-fold dilutions from 1 $IC_{50(2D\text{-}HepG2)}$ to 1/8 $IC_{50(2D\text{-}HepG2)}$ of each compound) demonstrated the synergistic effect of all concentrations (CI <1, Figure 3D–E). The cell viability of HepG2 cells at 1 $IC_{50(2D\text{-}HepG2)}$ to 1/4 $IC_{50(2D\text{-}HepG2)}$ of MSKE-DOX was lower than 50%. In fact, the concentrations of MSKE-DOX could be reduced from 1 $IC_{50(2D\text{-}HepG2)}$ to 1/4 $IC_{50(2D\text{-}HepG2)}$ to achieve 70% inhibitory effect against 2D-HepG2 cells (Figure 3D). In addition, the CI of MSKE-DOX was lower than 1 (CI <1, Figure 3E)) demonstrating the synergistic effect of the combinational treatment. In contrast, only PGG-DOX at 1 $IC_{50(2D\text{-}HepG2)}$ could exhibit 50% inhibitory effect against 2D-HepG2 cells. The CI of PGG-DOX was higher than 1 (CI >1, Figure 3E) presenting the antagonistic effect of the combinations. Thus, only the combination of MSKE and DOX was selected to study anticancer effects against 3D-HepG2 mono and coculture spheroids. Although PGG exhibited high potency against HepG2 cells, PGG could not increase the sensitivity of DOX in the combined therapy. It may be assumed that the 'Entourage effects' may take place where all phytochemical compounds in MKSE play a complementary role in anticancer activity rather than the single bioactive composition.

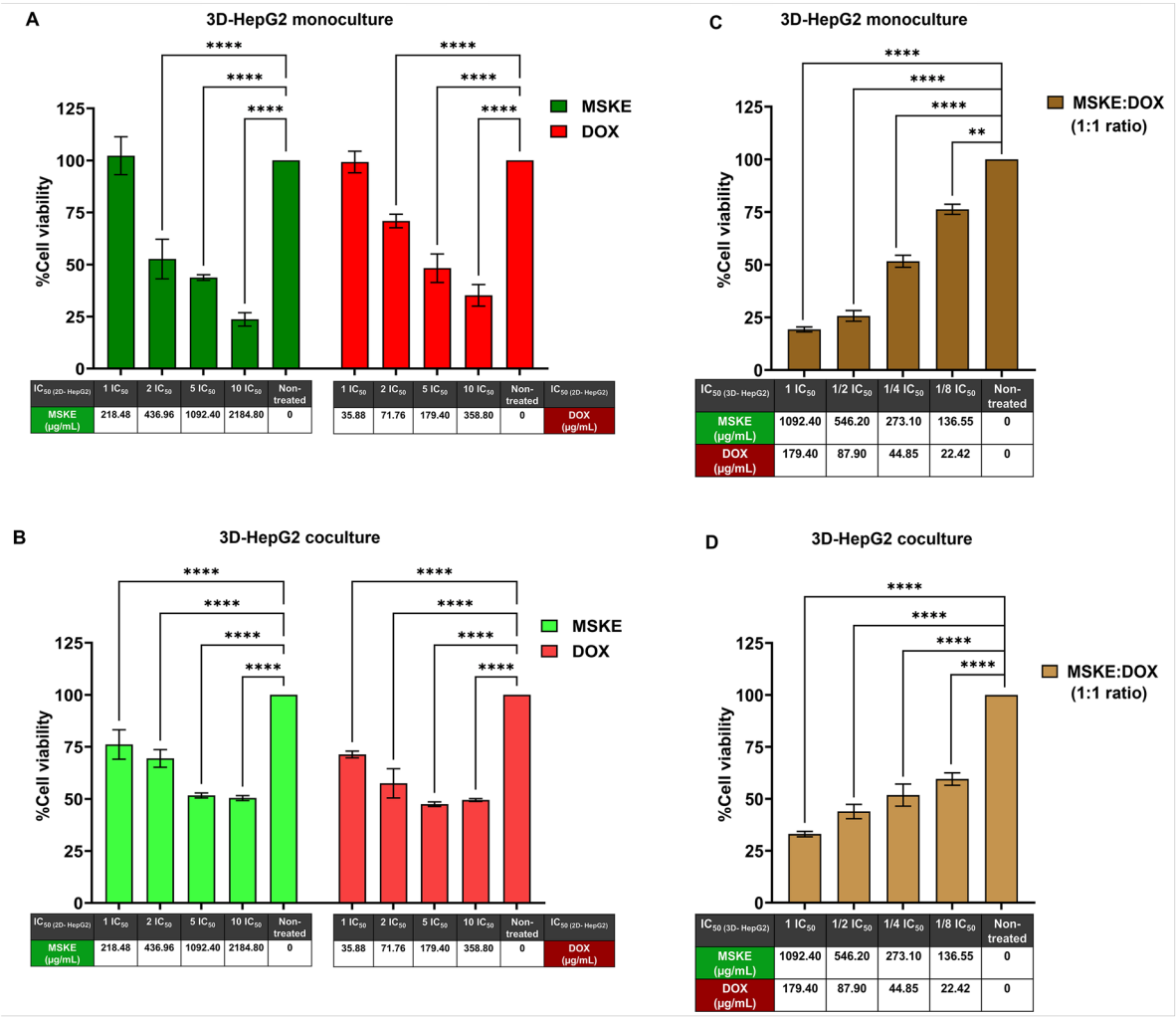

Figure 4. Anticancer activity of MSKE and DOX against mono and coculture 3D-HepG2 spheroids following 24 h exposure periods: % cell viability of 3D-HepG2 monoculture spheroids (A) and 3D-HepG2 coculture spheroids (B) after exposing to MSKE and DOX (1:1 ratio between MSKE:DOX) for 24 h at 1 IC_{50} - 10 IC_{50} based on IC_{50} of each active compound against 2D-HepG2 cells. % Cell viability of the combination therapy including MSKE-DOX against 3D-HepG2 monoculture spheroids (C) and 3D-HepG2 coculture spheroids (D) at 1 IC_{50} - 1/8 IC_{50} of each therapeutic agents ($n = 3$, mean ± SD).

Due to the presence of TME in 3D models, the concentration of chemotherapeutic drugs to achieve 50% inhibition was increased up to 2–3 times of $IC_{50(2D\text{-}HepG2)}$ (Song et al. 2016; Sae-be et al. 2023). To analyze the inhibitory effects of MSKE, DOX, and co-delivery of MSKE-DOX against 3D-HepG2 mono and coculture models, the concentrations of MSKE-DOX (Figure 4) were in the range between 1 to 10 times of $IC_{50(2D\text{-}HepG2)}$. The anticancer activities of both substances were in dose-dependent manners against 3D-HepG2 monoculture (Figure 4A). At dose 5 times of $IC_{50(2D\text{-}HepG2)}$, 1092.4 µg/mL of MSKE and 179.4 µg/mL of DOX, could decrease cell viability of 3D-HepG2 to be lower than 50%. While the viability of 3D-HepG2 coculture was reduced to 50% at doses 5 to 10 times of $IC_{50(2D\text{-}HepG2)}$ (Figure 4B). Thus, MSKE, 1092.4 µg/mL, and DOX, 179.4 µg/mL were selected as the IC_{50} values for the 3D-HepG2 model, to be used in combined therapy against 3D-HepG2 mono- and coculture spheroids. The concentrations of the combination therapy were, then, reduced by 2-fold dilutions; 1/2 to 1/8 $IC_{50(3D\text{-}HepG2)}$ of each compound, and the lowest concentrations were 136.55 µg/mL of MSKE and 22.42 µg/mL of DOX. The results of the combined therapy against 3D-HepG2 monoculture and coculture spheroids were demonstrated in Figure 4(C,D). The results illustrated that the combination of MSKE-DOX at the concentration of 1/4 (273.10 of MSKE and 44.85 µg/mL of DOX) reduced the viability of both 3D-HepG2 models to approximately 50%. Furthermore, the combination treatment at 1/2 to 1 IC_{50} resulted in a greater reduction, with cell viability below 50% in both 3D-HepG2 monoculture and coculture models. Thus, MSKE could be used as an adjuvant with DOX for

HCC treatment. To achieve maximum anticancer activities of each compound against 2D and 3D-HepG2 models, MSKE and DOX were selected to be separately loaded into HMSNs as drug carriers and designed as sequential treatment platform (SNP).

3.4. Toxicity of MSKE against 3D-imHC spheroids

The toxicity of MSKE against normal liver cells was examined using our in-house 3D-normal liver models fabricated by imHCs and HSCs (Sae-be et al. 2023). On day 10 after cell seeding, 3D-imHC coculture models were exposed to MSKE solutions at concentration range between 0 and 1,200 µg/mL (MSKE IC_{50} against 3D-HepG2 model is at 1092 µg/mL) for 24h. The % cell viability of 3D-imHC spheroids was higher than 90% while they were exposed to MSKE at concentrations between 0.5 and 250 µg/mL. On the contrary, the viability was reduced to 53.41% – 65.76% when exposed to MSKE at concentration 500–1,200 µg/mL (Figure S2), suggesting possible toxicity of MSKE on normal liver cells at higher doses. However, it has been reported *in vivo* studies that MSKE at doses 500–2,000 mg/kg body weight of rats could offer the hepatoprotective effect against liver damage induced by carbon tetrachloride (CCl_4) due to antioxidant and anti-inflammatory activities of main bioactive compounds (Nithitanakool et al. 2009). Recently, the ethanolic extract of MSKE at doses 250–1,000 mg/kg body weight of rats (*Mangifera indica* L. cv. Kaew Morakot) could prevent liver damage in rats with diabetic conditions and alleviate diabetes-induced pancreatic and liver oxidative damage by decreasing levels of malondialdehyde (Yoopum et al. 2023). The discrepancy between our *in vitro* result and the previous *in vivo* results may be due to the difference in objective studies and complexity between *in vitro* and animal models. As we are planning to carry on the *in vivo* study, therefore, we selected the dose range between 1/8 and 1 $IC_{50(3D\text{-}HepG2)}$ (Figure 4C,D and Figure S2) of the MSKE which exhibited subtoxic effect on the 3D-imHC spheroid models because such subtoxic effect has not been reported in an animal study at the same dose range. According to the hepatoprotective effect together with its anticancer effect the MSKE may be a good adjuvant therapy for hepatocellular carcinoma. We anticipated that the preliminary study for *in vivo* dose optimization to find the balance between hepatoprotective and anticancer activities are required before the beginning of our *in vivo* study.

3.5. HMSN synthesis, characterization, and drug encapsulation

HMSN synthesis was started by core seeding, mesoporous forming (Figure S3) and core solubilizing. The developed HMSNs in Figure 5(A) were spherical and highly monodisperse. The etching time and concentration of Na_2CO_3 are key parameters to be controlled in the etching process to achieve void volume in HMSNs for drug encapsulation (Chen et al. 2014; Kong et al. 2017). The average particle size of HMSNs was 73.58 ± 6.16 nm. While the HD and PDI of HMSNs measured by DLS were found to be at 173.3 ± 2.1 nm (Figure 5B) and 0.113 ± 0.025 (TableS 1), respectively. The surface charge density of non-encapsulated HMSNs was observed at −30.0 ± 2.06 mV. FT-IR showed the functional groups at 800 and 1100 cm^{-1}, which presented symmetric stretching vibration and asymmetric stretching vibration of siloxane groups (Si-O-Si), respectively, and silanol groups (Si-OH) at 900 and 3400 cm^{-1} were the symmetrical stretching vibration and bending vibration, respectively (Figure 5C). In addition, after extraction, CTAC was thoroughly removed where the peak of -CH- (at 2900 and 3000 cm^{-1}) of CTAC disappeared as shown in Figure 5(C) (Kong et al. 2017). The BET analysis demonstrated that the surface area of HMSNs was 1280.10 m^2/g. Isotherm of HMSNs was typical Langmuir IV hysteresis loops, indicating the existence of uniform mesopore structures. The pore volume and diameter of HMSNs were 2.35 cm^3/g and 3.93 nm, respectively (Figure 5D,E). GQDs presented maximum excitation and emission at 417.0 and 531.0 nm, respectively and the electron diffraction image revealed the crystalline structure of the graphene (Figure S4). Size of GQDs was found to be 7.05 ± 0.69 nm by TEM (Figure 5F). To cap GQDs on HMSN surface, firstly, HMSNs were modified surface with amine groups (NH_2; NH_2HMSNs). The bending vibration of -NH group of primary amines at the peaks of 1490 and 1560 cm^{-1} was observed in the FT-IR spectra of NH_2HMSNs (Figure 5C). Next, GQDs were activated by EDC and NHS for at least 4 h before adding resuspended NH_2HMSNs. The GQDs were capped on NH_2HMSNs surface (GQD-NH_2HMSNs) through amide bonds between the carboxyl group on GQDs and the amino group on HMSNs. FT-IR demonstrated -CONH- at 1580 cm^{-1} (Figure 5C)

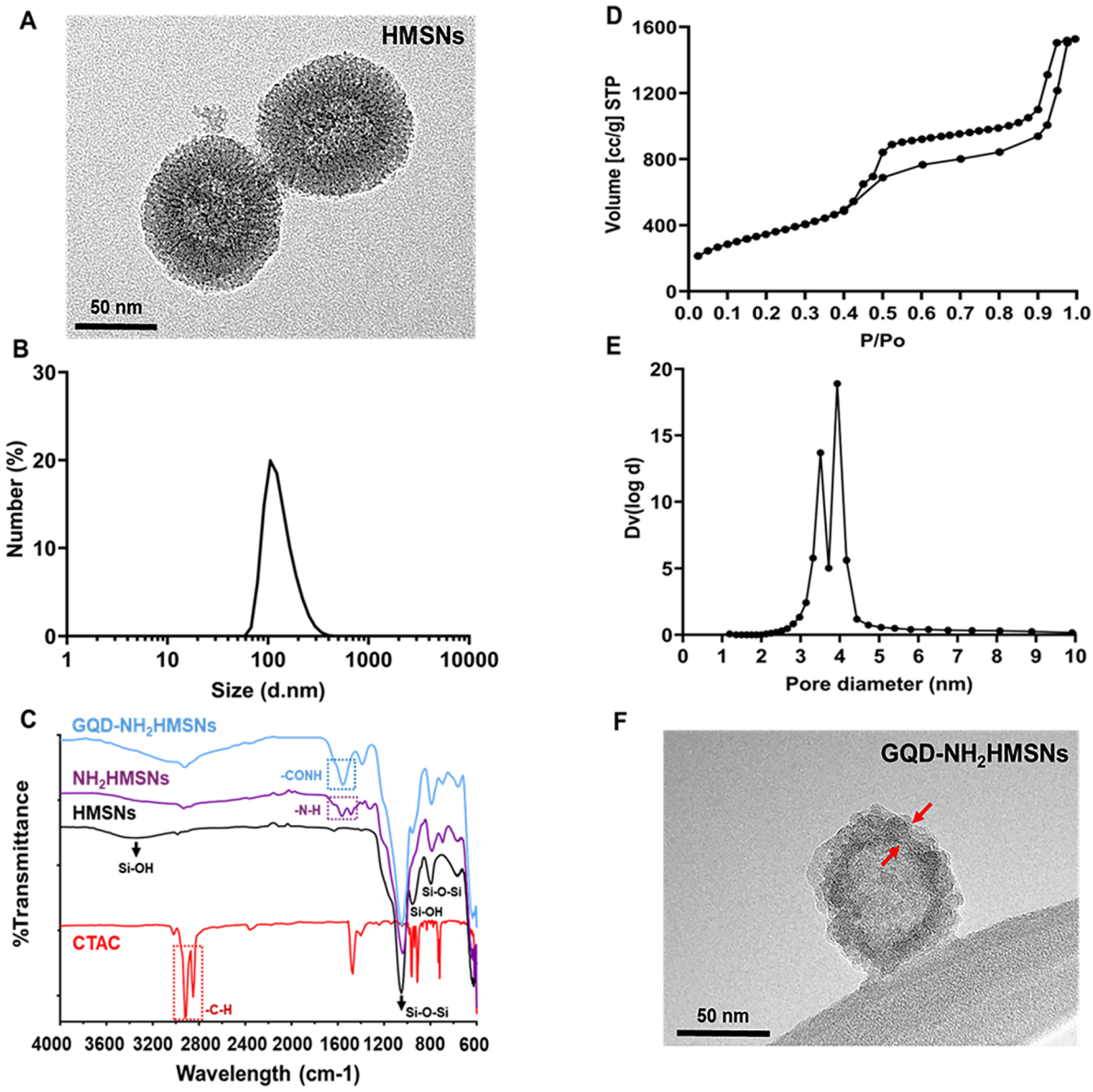

Figure 5. Physicochemical characterization of HMSNs and GQD-HMSNs: TEM images of HMSNs (A) and hydrodynamic diameter (HD) of HMSNs (B). FT-IR of CTAC, HMSNs after extraction by HCl-ethanol solution GQDs capped HMSNs (C). Nitrogen adsorption-desorption isotherms by BET (D) and pore size distribution of HMSNs (E). The GQD-capped on the surface of NH_2HMSNs *via* amide linkage observed using TEM (F, red arrows).

and TEM showed GQDs to seal the mesoporous pore (Figure 5F). In addition, the particle size, 78.02 ± 4.97 nm, of GQD-NH_2HMSNs was slightly larger than that of HMSNs suggesting the capping of GQD on the surface of HMSNs.

Electrostatic interactions facilitate the incorporation of positively charged DOX within negatively charged HMSNs in Figure 6(A) (Gao et al. 2011). The presence of DOX was indicated by FT-IR in Figure 6(B). The average particle diameters of DOX-HMSNs were 94.99 ± 6.30 nm. Meanwhile, the HD and surface charge density of DOX-HMSNs were observed at 221.3 ± 2.6 nm and 19.3 ± 1.0 mV (Figure 6C,D), respectively. The %EE and %LD of DOX were 96.42 ± 2.48 and 29.0 ± 0.70% (Table S1), respectively. While NH_2 and Si-O-Si groups of NH_2HMSNs could enhance MSKE encapsulation by hydrogen bonds (H-bonds) with hydroxyl (-OH) and carbonyl groups (-C = O-) of PGG. Furthermore, the NH_2 could form amide bonds (-CONH-) with -COOH- of GQDs through carbodiimide reaction in Figure 6(E,F) (Kong et al. 2017; Yao et al. 2017). The TEM image in Figure 6(E) showed spherical shapes of GQD-MSKE-NH_2HMSNs with an average particle diameter of 96.12 ± 5.12 nm. The HD and zeta potential of GQD-MSKE-NH_2HMSNs were 226.0 ± 1.0 nm and 33.87 ± 2.44 mV (Figure 6D), respectively. The %EE and %LD of MSKE loaded into

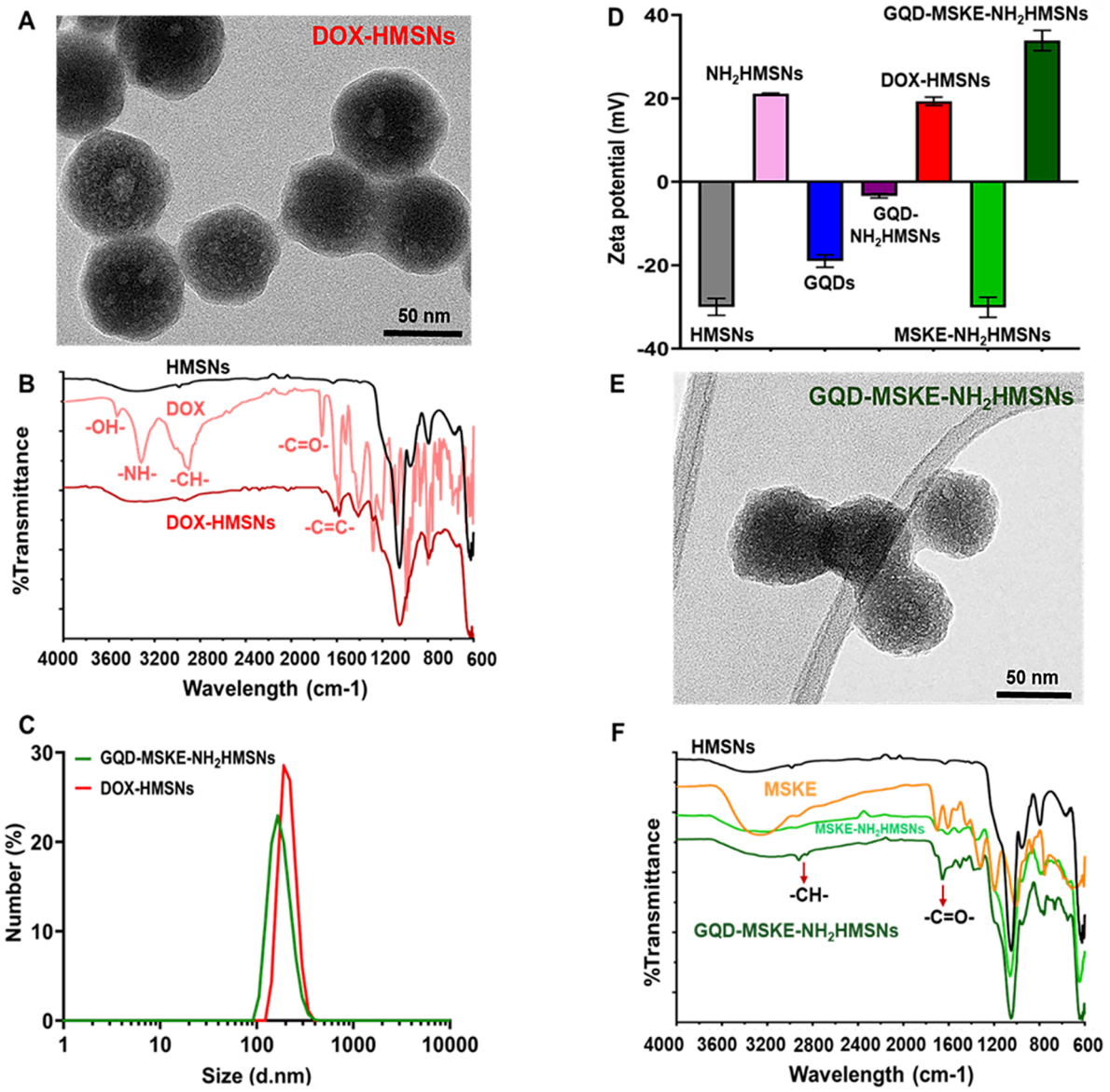

Figure 6. Physicochemical characterization of DOX-HMSNs and GQD-MSKE-NH_2HMSNs: TEM image of DOX-HMSNs (A), FT-IR of DOX-HMSNs, compared to HMSNs and DOX (B), hydrodynamic diameter (HD) of DOX-HMSNs and GQD-MSKE-NH_2HMSNs (C), zeta potential of HMSNs, NH_2HMSNs, GQD-NH_2HMSNs, DOX-HMSNs, MSKE-NH_2HMSNs and GQD-MSKE-NH_2HMSNs (D, $n = 3$, mean ± SD), TEM image of GQD-MSKE-NH_2HMSNs (E) and FT-IR of GQD-MSKE-NH_2HMSNs, compared to HMSNs, MSKE, and MSKE-NH_2HMSNs (F).

GQD-MSKE-NH_2HMSNs calculated using PGG were 95.50 ± 0.20 and 46.72 ± 1.14% (GQD-MSKE-NH_2HMSNs) (Table S1), respectively.

3.6. Photothermal performance of GQD-MSKE-NH_2HMSNs

GQDs could efficiently convert NIR light into heat (thermal energy) (Dar et al. 2023). The photothermal efficiency of GQD-MSKE-NH_2HMSNs was evaluated. The temperature change of GQD-MSKE-NH_2HMSNs was monitored and recorded by NIR camera with a thermometer every 1 min and deionized (DI) water was used as the control. Suspensions of GQD-MSKE-NH_2HMSNs at varying concentrations (0.1, 0.25, 0.5, and 1.0 mg/mL) were irradiated with 785 nm NIR light at a power density of 3.0 W/cm^2 for 10 min. As shown in Figure 7(A), the temperature of GQD-MSKE-NH_2HMSNs increased rapidly under continuous NIR irradiation and the increase in temperature was dependent of the concentrations of the GQD-MSKE-NH_2HMSNs. At a fixed concentration (0.5 mg/mL), the photothermal performance correlated with laser

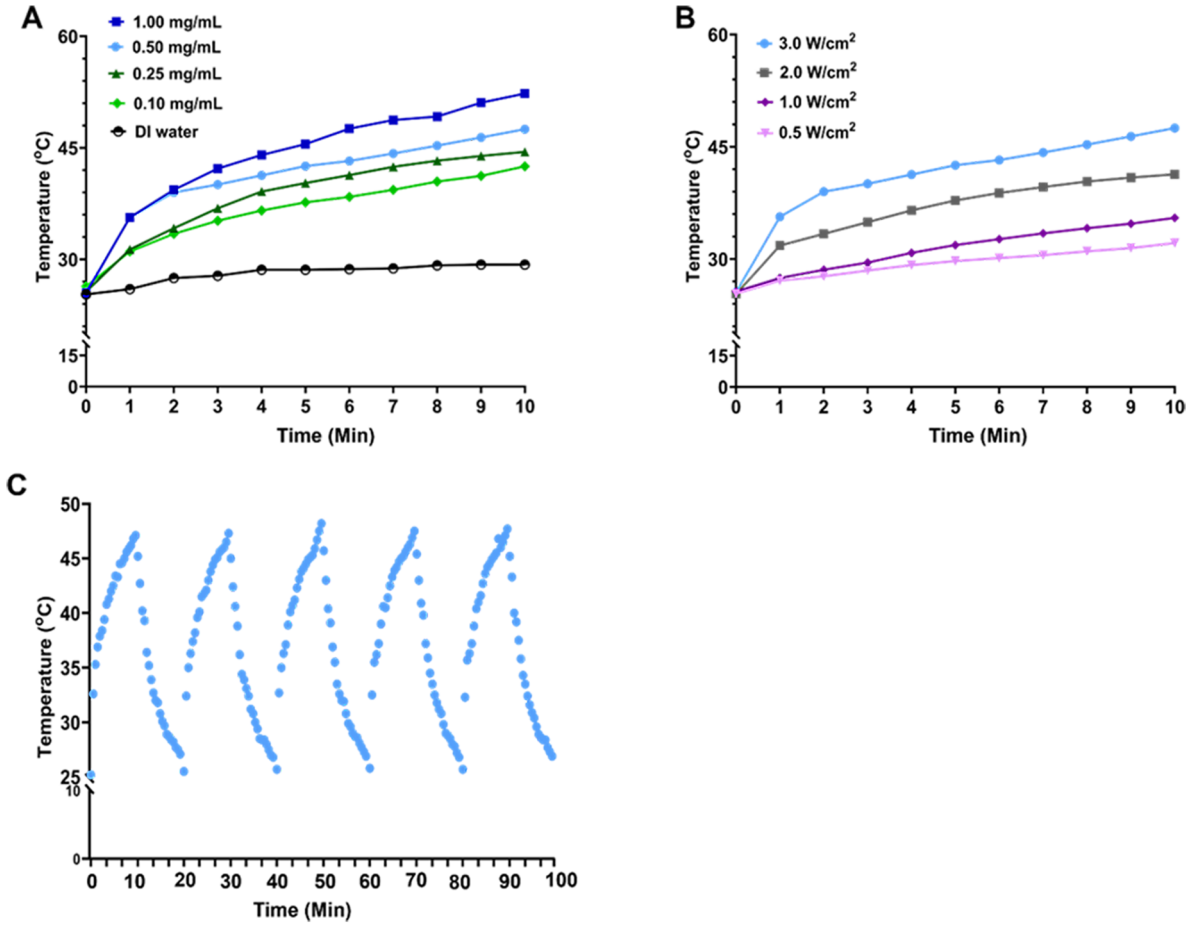

Figure 7. *In vitro* photothermal performance and stability of GQD-MSKE-NH_2HMSNs: Photothermal heating curve of GQD-MSKE-NH_2HMSNs suspension at different concentrations (0.10, 0.25, 0.50 and 1.00 mg/mL) and DI water (as control) using 785 nm laser irradiation, 3.0 W/cm^2 for 10 min (A). Photothermal heating curve of GQD-MSKE-NH_2HMSNs, 0.5 mg/mL, at different powers (3.0, 2.0, 1.0 and 0.5 W/cm^2) for 10 min (B). The photothermal stability of GQD-MSKE-NH_2HMSNs at 0.5 mg/mL after exposing continuous 785 nm laser with 3.0 W/cm^2 (5 cycles of on-off laser) (C, $n = 3$, mean ± SD).

power intensity, as illustrated in Figure 7(B). Furthermore, the photostability of GQD-MSKE-NH_2HMSNs at 0.5 mg/mL was studied by five cycles of laser irradiation (Figure 7C). As observed in Figure 7(C), almost no noticeable attenuation was observed after five cycles of laser irradiation. Therefore, GQD-MSKE-NH_2HMSNs had good photothermal stability and would be a promising photothermal agent for PTT.

3.7. Drug release study

The release of DOX from DOX-HMSNs was observed for 48 h (Figure 8A). Two conditions, pH 5.0 and pH 7.4 simulated intracellular conditions of cancer cells and physiological conditions, respectively. The results demonstrated the prompt release of DOX at 2 h resulting from the dissolution of DOX that bound to the surface of the particles or entrapped in the mesopores. The cumulative release of DOX at T = 48 h, pH 5.0, and 7.4 were 0.112 mg (20.55% of loaded DOX) and 0.041 mg (2.42% of loaded DOX). Therefore, *in vitro* drug release profile of DOX-HMSNs exhibited pH-responsive drug release (pH 5.0 > pH 7.4, ****$p \leq 0.0001$). DOX release process was due to the protonation of silanol groups (-Si-OH) within the HMSNs at the acidic pH. This protonation could decrease the electrostatic interactions between DOX and HMSNs initiating the dissociation of DOX (Gao et al. 2011; Moghaddam et al. 2018). The DOX-HMSNs exhibited pH-responsive drug release at an acidic condition (pH 5.0) which was exploited to passively release drugs into HepG2 cells.

The percentage release of MSKE from GQD-MSKE-NH_2HMSNs observed for 48 h could be detected at 6.13% and 20.19% of loaded MSKE at pH 5.0 and pH 7.4, respectively (Figure 8A). The cumulative

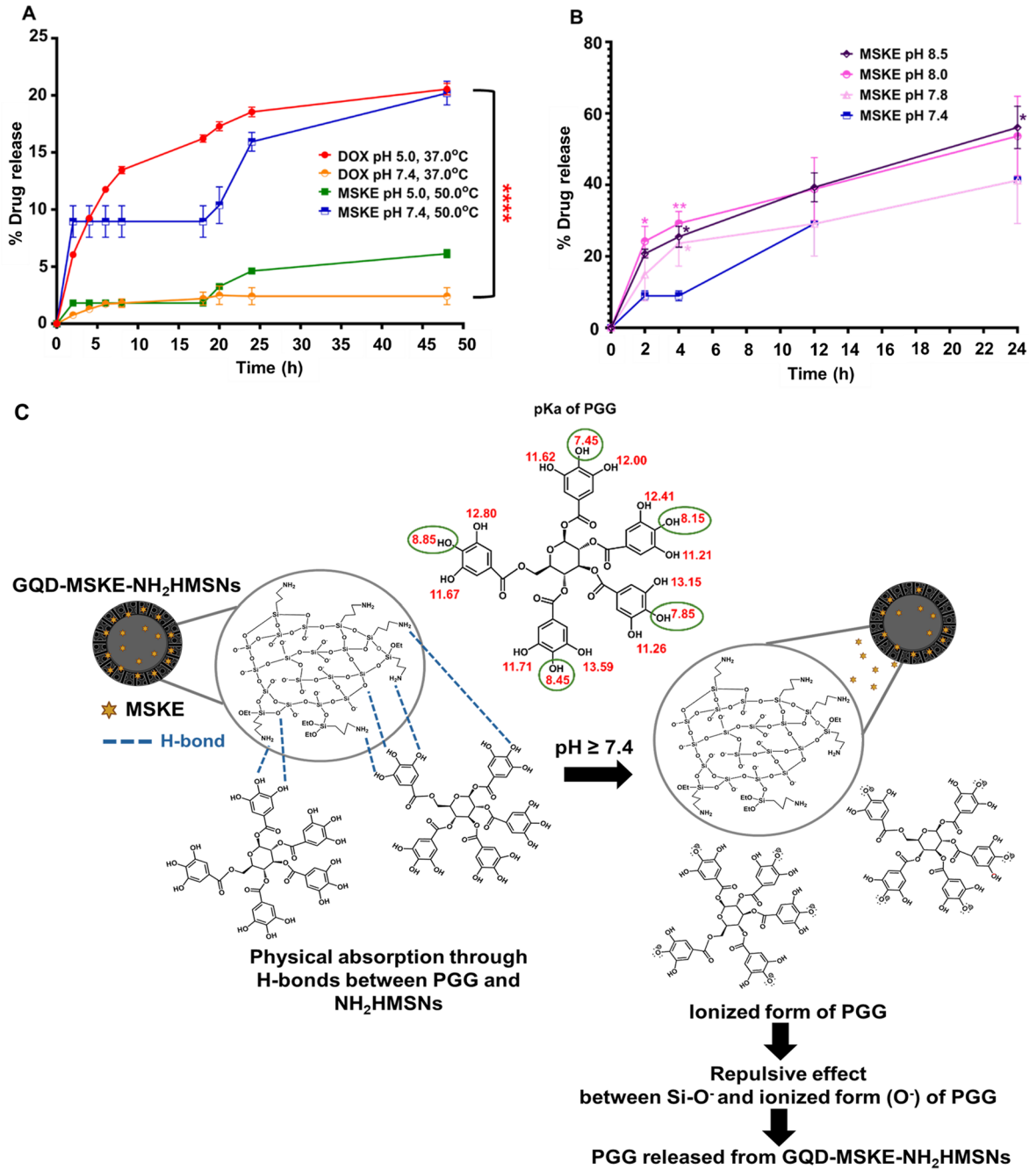

Figure 8. *In vitro* drug release of DOX-HMSNs and GQD-MSKE-NH_2HMSNs: the cumulative release of DOX from DOX-HMSNs and PGG from GQD-MSKE-NH_2HMSNs for 48 h at pH 5.0 and 7.4, respectively (the release of DOX at pH 5.0 > pH 7.4, ****$p \leq 0.0001$) (A). The release profile PGG from GQD-MSKE-NH_2HMSNs for 24 h at pH 7.4, 7.8, 8.0, and 8.5, respectively (B, $n = 3$, mean ± SD, *$p \leq 0.05$, **$p \leq 0.01$). pKa of PGG and release mechanism of MSKE from GQD-MSKE-NH_2HMSNs at pH ≥ 7.4 depending on protonation of MSKE (C). The particles of GQD-MSKE-NH_2HMSNs were created with biorender.com.

release of MSKE at 6.13% (pH 5.0) and 20.19% (pH7.4) of MSKE from GQD-MSKE-NH_2HMSNs was further calculated and found that these concentrations are sufficient to kill cancer cells in combination with DOX-HMSNs. The predicted pKa of PGG analyzed using MarvinSketch software (version 22.9, Chemaxon) could be used to explain the drug release mechanism following Henderson–Hasselbalch equation (Figure 8B,C). Hydroxy groups (-OH) at para position of PGG (Figure 8C, green circle) are deprotonated when pH is higher than pKa initiating the release of the MSKE. At pH 5.0, most PGG became unionized

form without releasing. In contrast, at pH 7.4 or higher, OH group of PGG was deprotonated. The ionized form of the PGG was released due to the repulsive effect between the negative charge of the ionized PGG and Si-O-Si groups in HMSNs. The results of drug release at pH ≥ 7.4 were demonstrated in Figure 8(B). Similarly, PGG loaded poly(lactide-co-glycolide) nanoparticles (PLGA NPs) exhibited burst release in PBS (pH 7.4) during the first 24 h, followed by the sustainable release for 1 week (Arnold et al. 2021).

Additionally, according to the design of GQD-MSKE-NH_2HMSNs, the nanoparticles were passively targeted to tumor and cancer cells. The nanosized, 96.12 ± 5.12 nm (TEM result), of GQD-MSKE-NH_2HMSNs could reach tumor passively *via* fenestration of tumor blood vessels. As the leaky blood vessels are only present in tumor, the GQD-MSKE-NH_2HMSNs are likely to extravasate to cancer cells more than normal cells. Once the GQD-MSKE-NH_2HMSNs enter the cancer cells, their amine-surface modifification provided ability to escape endosome at acidic condition through proton sponge effect and release active MSKE in cytosol of cancer cells. Although the release of the GQD-MSKE-NH_2HMSNs is not pH sensitive, the prompt release of MSKE could be observed at pH 7.4 (Figure 8A). Subsequently, the release of MSKE could also be activated by NIR irradiation at the tumor site. The elevated temperature could cause structural changes in graphene gatekeeper and cleave amide bonds (linking between the carrier and GQD) allowing the release of MSKE from the pore. The external stimuli of NIR could initiate localized hyperthermia for cancer treatment. Therefore, we proposed that the GQD-MSKE-NH_2HMSNs should be administered *via* intratumoural (IT) injection. The passive targeting strategy of the GQD-MSKE-NH_2HMSNs together with its sustained release profile can compromise the MSKE-DOX synergy and targeting ability as can be seen from their cellular internalization (Figure 11) and anticancer activity (Figure 12).

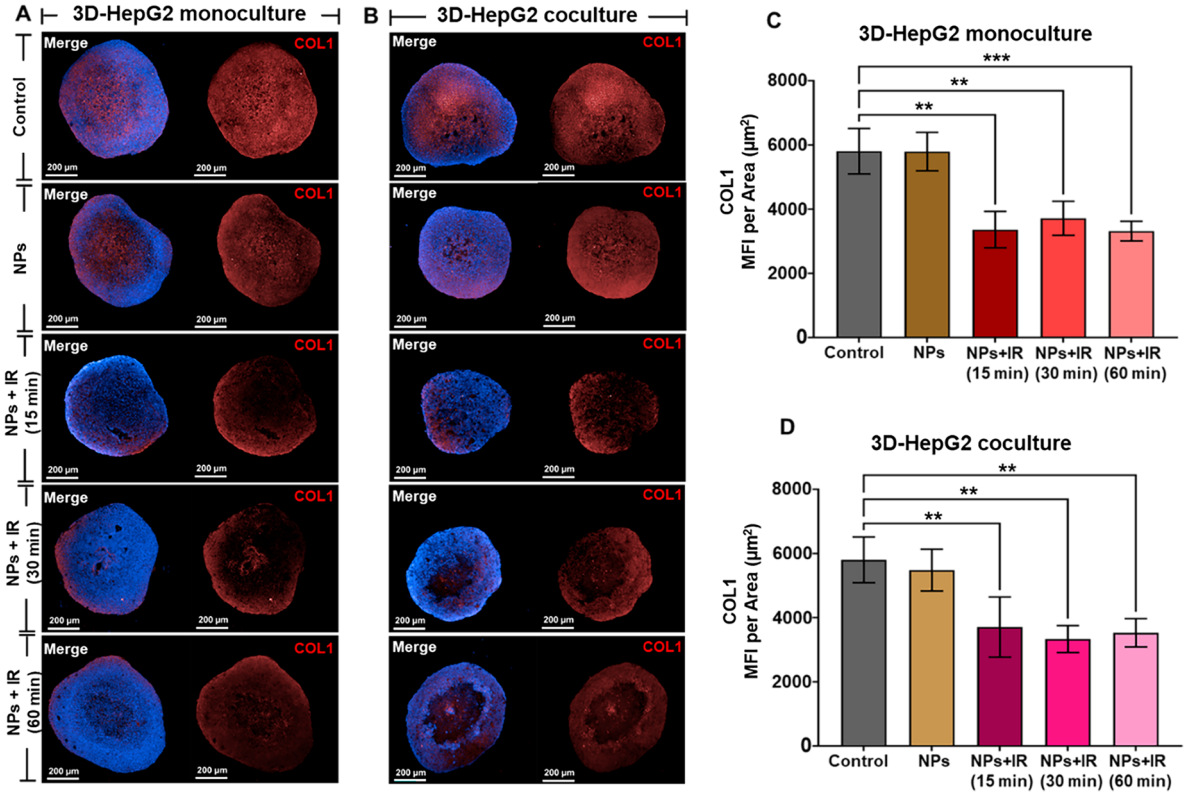

Figure 9. Collagen depletion in 3D-HepG2 model: Confocal fluorescent images (maximum projection) demonstrated the distribution of COL1 (red) in 3D-HepG2 monoculture (A) and coculture (B) at day10 after seeding. The intensity of COL1 was measured after irradiation (laser condition: 785 nm laser irradiation, 3.0 W/cm^2 for 10 min) for 15, 30 and 60 min compared with the non-treated group (C–D) ($n = 3$, mean ± SD, $^{**}p \leq 0.01$, $^{***}p \leq 0.001$). Nuclei were stained in blue of Hoechst33342 and COL1 (collagen type I) was stained in red. Noted: Merge = hoechst 33342 (blue) + COL1 (red).

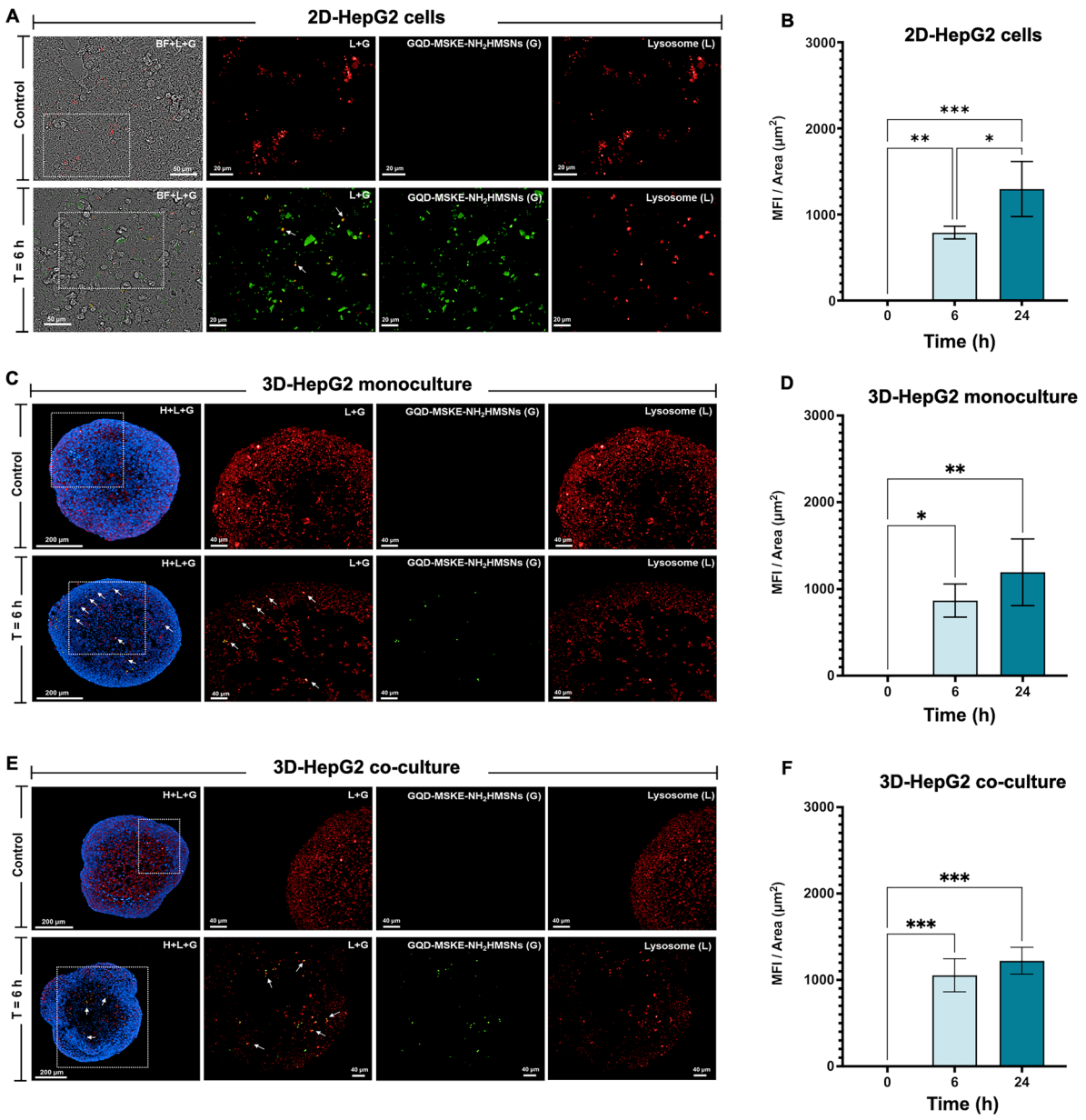

Figure 10. *In vitro* cellular internalization of GQD-MSKE-NH_2HMSNs (green): confocal fluorescent images demonstrated cellular uptake of non-treated (without nanoparticles; control) and treated groups following exposure to GQD-MSKE-NH_2HMSNs (0.1 mg/mL). In 2D-HepG2 cells, GQD-MSKE-NH_2HMSNs localized within lysosomes (A), with the mean fluorescence intensity (MFI) per area (μm^2) significantly increasing over time after 6 and 24 (Figure S5) hours of incubation (B) ($n = 3$, mean ± SD, $^*p \leq 0.05$, $^{**}p \leq 0.01$, and $^{***}p \leq 0.001$). Furthermore, GQD-MSKE-NH_2HMSNs were able to penetrate and accumulate in lysosomes of 3D-HepG2 monoculture (C) and 3D-HepG2 coculture (E) at T = 6 h. The corresponding MFI per area (μm^2) of GQD-MSKE-NH_2HMSNs within the 3D-HepG2 monoculture and coculture models is shown in D and F, respectively ($n = 3$, mean ± SD, $^*p \leq 0.05$, and $^{***}p \leq 0.001$). The white square in the left column indicated the region of interest (ROI) that was magnified in each channel. Nuclei were stained in blue of Hoechst33342 (H), acidic environment in lysosome was stained in red of acridine orange (L), GQD-MSKE-NH_2HMSNs presented strong green fluorescence (G) and yellow (merge red and green; white arrows) demonstrated co-localization of GQD-MSKE-NH_2HMSNs into lysosome. Noted: BF = bright field.

3.8. Collagen depleting in 3D-HepG2 spheroids by NIR laser

Majority of HCC has been developed from chronically damaged liver tissue, the ECM known as collagen type I (COL1) produced from activated HSCs abundantly found in fibrotic liver (Yin et al. 2013; Song et al. 2016). COL1 plays a decisive role as a biological barrier to obstruct the penetration of NPs. Thus, the

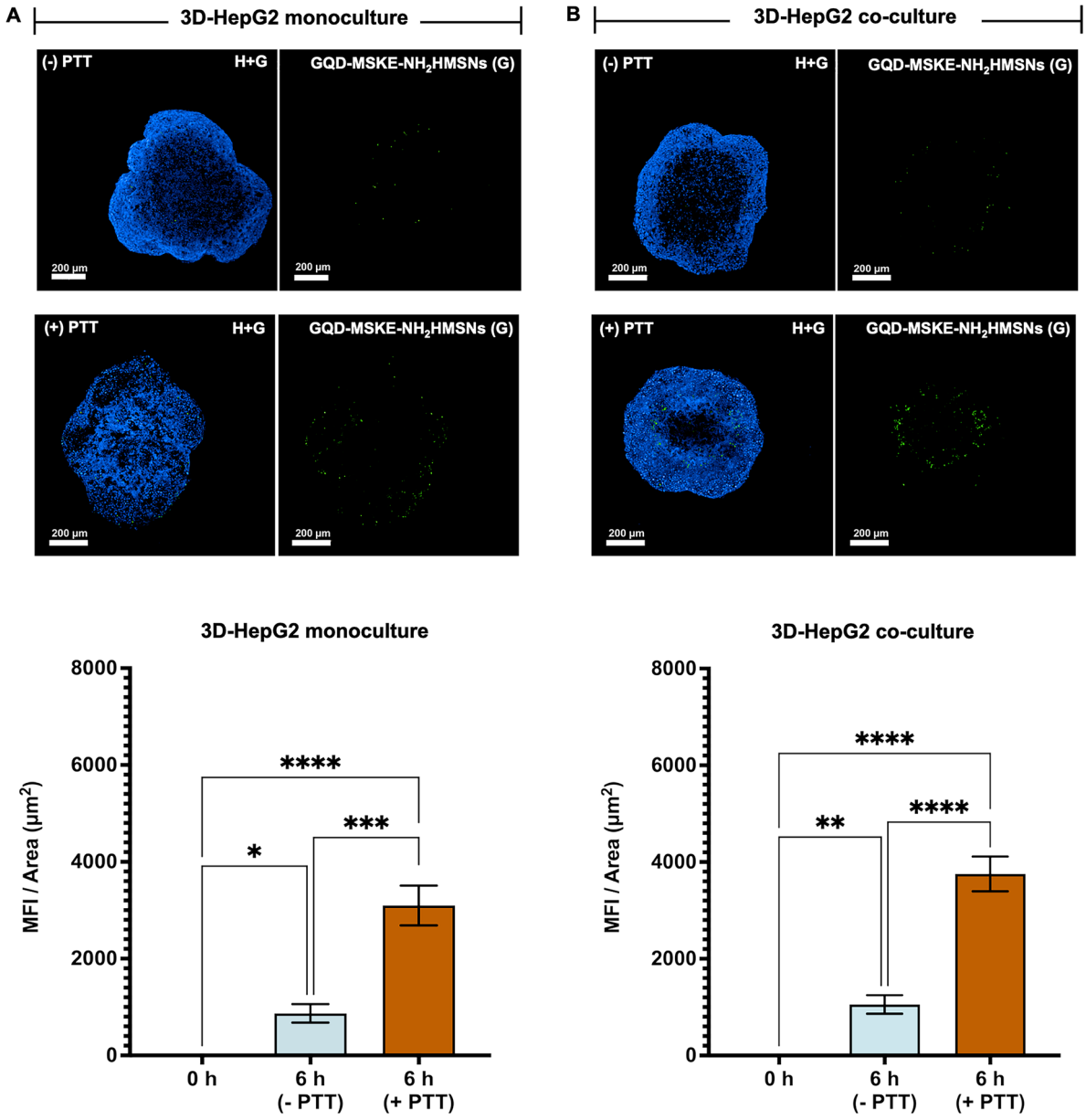

Figure 11. *In vitro* cellular internalization of GQD-MSKE-NH_2HMSNs (green) without (-) and with (+) PTT using 3D spheroid models: Confocal fluorescent images demonstrated cellular uptake of GQD-MSKE-NH_2HMSNs (0.1 mg/mL) after the treatment with and without PTT. The MFI per area (μm^2) of GQDs in 3D-HepG2 monoculture (A) and coculture spheroids (B) was quantified ($n = 3$, mean ± SD, ***$p \leq 0.001$, ****$p \leq 0.0001$). Following the PTT, GQD-MSKE-NH_2HMSNs were able to penetrate deeper into the spheroid core, resulting in a significantly higher MFI per area compared to the non-PTT group in both 3D models. Noted: Nuclei were stained in blue of Hoechst33342 (H).

decrease in COL1 could enhance the penetration of NPs providing the maximum therapeutic efficacy. PTT has been broadly used for combination therapy because PTT could reduce stiffness of ECM (Marangon et al. 2017) and increase the sensitivity of cancer cells to chemotherapy (Bhatt et al. 2023). Both 3D-HepG2 mono and coculture spheroids were exposed to 0.5 mg/mL of GQD-MSKE-NH_2HMSNs for 6 h before NIR irradiation (at 785 nm, 3.0 W/cm^2) for 10 min. After irradiation for 15, 30, and 60 min, the results confirmed that PTT could reduce the integrity of COL1 (red fluorescence in Figure 9A,B) within the spheroids. The difference in the waiting period before imaging (15, 30, and 60 min) showed no significant effect on the reduction of COL1 (Figure 9C,D). The intensity of COL1 in the PTT treatment group was significantly lower than the control group in Figure 9(C,D). Therefore, this study confirmed that PTT could increase the penetration of NPs into the tumor.

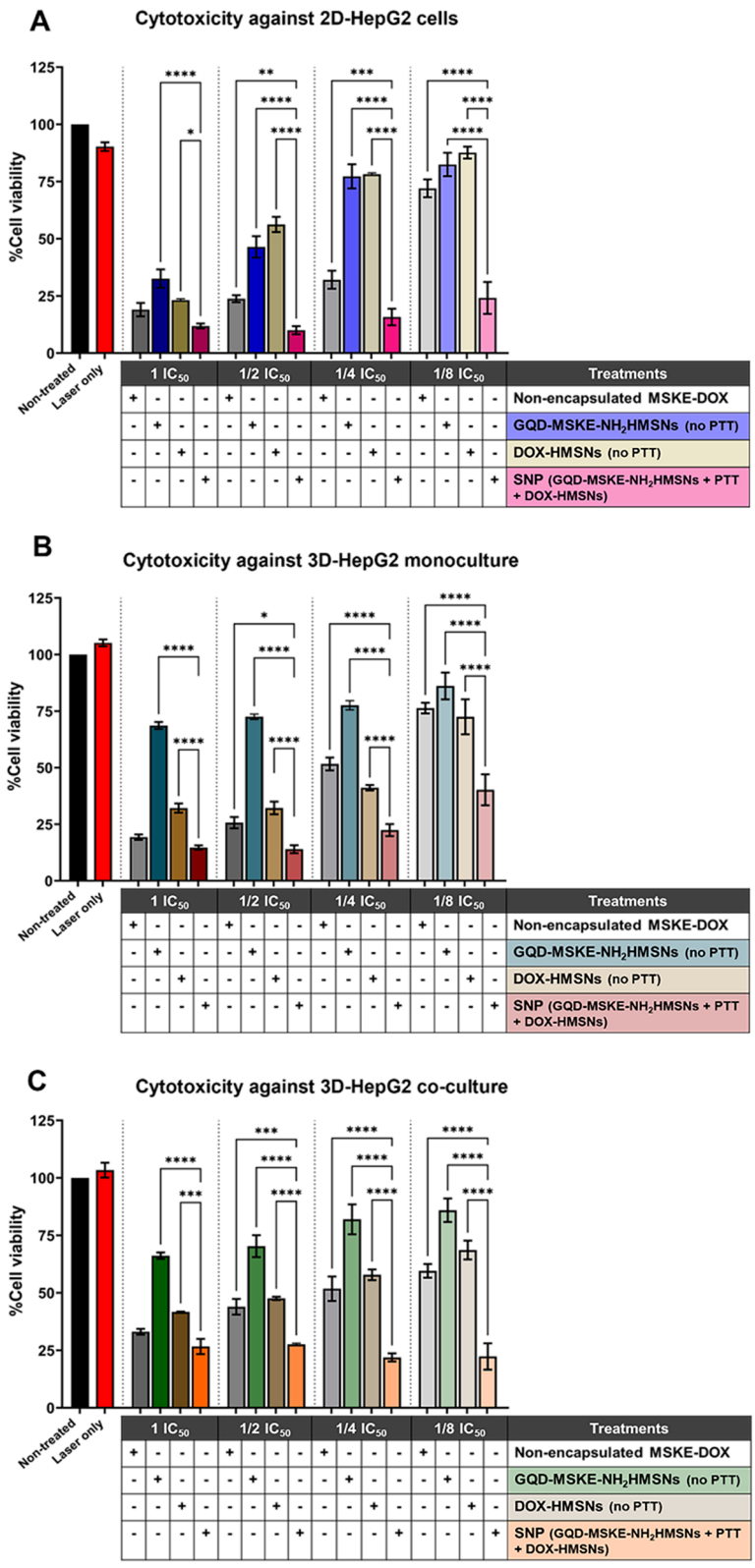

Figure 12. *In vitro* anticancer activity of the individual treatments of either GQD-MSKE-NH_2HMSNs or DOX-HMSNs, and the combined treatment of SNP against HepG2 models: the inhibitory effect of non-encapsulated MSKE-DOX, encapsulated MSKE (GQD-MSKE-NH_2HMSNs without PTT), encapsulated DOX (DOX-HMSNs without PTT) and SNP against 2D-HepG2 cells (A), 3D-HepG2 monoculture (B) and 3D-HepG2 coculture spheroids (C), respectively ($n = 3$, mean ± SD, $^*p \leq 0.05$, $^{**}p \leq 0.01$, $^{***}p \leq 0.001$, $^{****}p \leq 0.0001$).

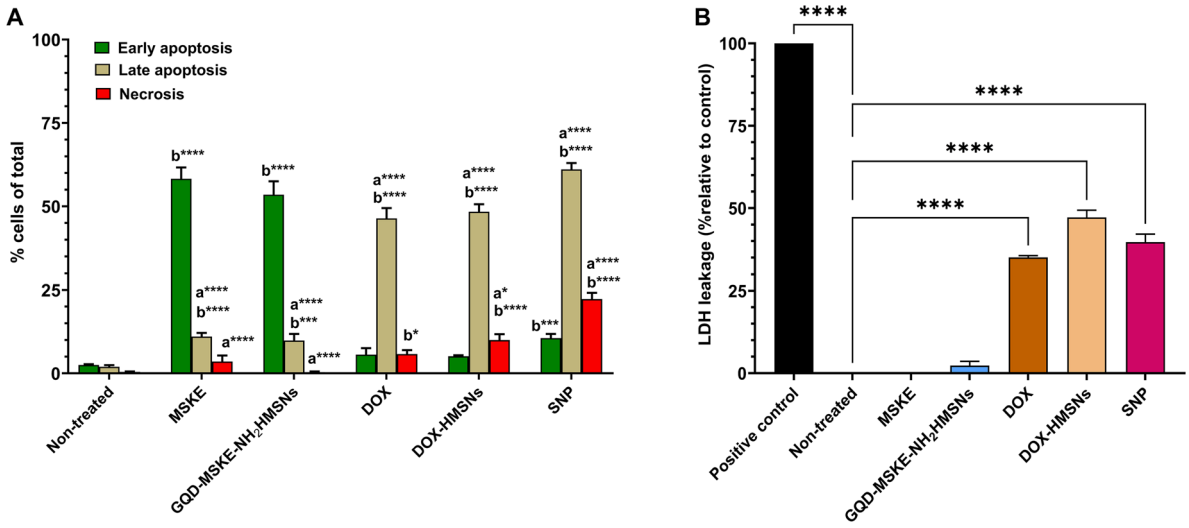

Figure 13. Cell death mechanisms assessed by apoptotic and LDH assays: the percentage of HepG2 cells undergoing apoptosis or necrosis after treatment with non-encapsulated drugs (MSKE, DOX), single-platform encapsulated drugs (GQD-MSKE-NH_2HMSNs, DOX-HMSNs), and the SNP, as determined by Annexin V-FITC/PI staining (A). The letters a and b indicate statistically significant differences within treatment groups (early apoptosis (as control), late apoptosis, and necrosis) and between treatment groups compared to the non-treated (as control), respectively. LDH release from HepG2 cells following treatment, indicating membrane damage (B) ($n = 3$, mean ± SD, $^{*}p \leq 0.05$, and $^{****}p \leq 0.0001$).

3.9. Cellular uptake of NPs

Passive targeting could facilitate the accumulation of NPs in tumor areas and cancer cells. *In vitro* cellular uptake of GQD-MSKE-NH_2HMSNs (0.1 mg/mL) was investigated in both 2D and 3D-HepG2 models after 6 (Figures 10 and 11) and 24h (Figure S5) of the incubation, without (Figure 10) and with laser irradiation (Figure 11). The inherent green fluorescence of GQDs enabled real-time imaging and monitoring of cellular uptake, while red fluorescence of AO, corresponding to lysosomal compartment, indicated subcellular localization. The results exhibited that GQD-MSKE-NH_2HMSNs were internalized *via* endocytosis (yellow in Figure 10A) and predominantly accumulated in lysosomes in both 2D and 3D-HepG2 models (Figure 10). Without PTT, the accumulation of most GQD-MSKE-NH_2HMSNs was primarily observed at the periphery of the spheroids. Quantitative analysis of MFI per area (μm^2) revealed a time-dependent increase in particle uptake in the 2D and 3D-HepG2 models over 24 hours. The variation of distribution may be observed in the 3D models due to the physical and biological barriers in the spheroids compared with the 2D model (Priwitaningrum et al. 2016). However, after irradiation (+PTT), COL1 integrity distributed within the 3D-HepG2 models was reduced (see results in Section 3.8), leading to significantly enhanced and deeper penetration of GQD-MSKE-NH_2HMSNs compared with the non-irradiated group (-PTT) (Figure 11A,B, $^{***}p \leq 0.001$, and $^{****}p \leq 0.0001$, $n = 3$). These findings suggest that PTT can effectively enhance nanoparticle distribution within the core of 3D tumor models.

3.10. Anticancer activity of DOX-HMSNs, GQD-MSKE-NH_2HMSNs, and SNP against 2D-HepG2 cells and 3D-HepG2 spheroids

The sequential delivery system incorporating PTT for ECM remodeling followed by chemotherapeutic drug administration has been extensively explored (Huang et al., 2022). Pretreatment modulation of the TME including ECM reconstruction, reduction of hypoxia, and increase in vascular permeability has been shown to enhance the therapeutic efficacy of anticancer agents (Shim et al. 2017). In this study, SNP consisting of GQD-MSKE-NH_2HMSNs and DOX-HMSNs provided a triple combination therapy (Adjuvant-PTT-Chemo). GQD-MSKE-NH_2HMSNs acted as the pretreatment agent, delivering both the MSKE adjuvant and initiating PTT. Subsequently, DOX-HMSNs were administered to exert anticancer effects. The anticancer efficacy of single treatments (DOX-HMSNs or GQD-MSKE-NH_2HMSNs) and the SNP was evaluated in both 2D-HepG2 cells and 3D-HepG2 spheroids using WST-1 assay (Figure 12A–C). Results demonstrated that

PTT alone and unloaded SNP did not significantly reduce cell viability in either 2D or 3D models ($p > 0.05$; Figure 12 and S6). Interestingly, the SNP treatment, at concentrations ranging from 1/2 to 1/8 of the $IC_{50(2D\text{-}HepG2)}$, significantly inhibited cell viability by up to 70% (**$p \leq 0.01$, ***$p \leq 0.001$, ****$p \leq 0.0001$, $n = 3$; Figure 12A). Similarly, inhibitory effects were observed in both 3D-HepG2 monoculture and coculture spheroids. The SNP treatment at ratio 1/2 to 1/8 $IC_{50(3D\text{-}HepG2)}$, exhibited significantly greater anticancer activity than either individual treatment or the combination of non-encapsulated MSKE and DOX (Figure 12B,C; *$p \leq 0.05$, ***$p \leq 0.001$, ****$p \leq 0.0001$, $n = 3$), indicating a synergistic effect (MSKE-PTT-Chemo). GQD-MSKE-NH_2HMSNs exerted a dual primary effect by delivering MSKE to cancer cells and simultaneously facilitating PTT to enhance nanoparticle penetration (Marangon et al. 2017). In addition, pH-responsive stimuli of DOX-HMSNs assisted selective drug release within the acidic TME (Gao et al. 2011). As a result, the sequential triple combination therapy allowed a reduction in the required doses of DOX and MSKE by 50% in 3D-HepG2 monoculture spheroids and by 75% in coculture spheroids, compared to cells treated with individual, non-encapsulated nanoparticles.

Treatment effect of individual and SNP treatments on spheroid size is illustrated in Figure S7. In the control non-treated in all treatment groups both mono- and coculture models, the diameters of 3D-HepG2 spheroids increased over time, indicating active proliferation of viable cells (Figure S7A–C). In contrast, DOX treatment group has been reported to disrupt spheroid integrity in a concentration- and time-dependent manner (Kim et al. 2010; Namgung et al. 2024). Treatment with DOX-HMSNs at $1IC_{50}$ resulted in only a slight increase in spheroid diameter (Figure S7(A), corresponding with the lowest cell viability compared to 1/8 IC_{50} to 1/2 $IC_{50\ (3D\text{-}HepG2)}$. Interestingly, 3D-HepG2 coculture spheroids treated with low doses at range 1/8 IC_{50} to 1/2 $IC_{50\ (3D\text{-}HepG2)}$ significantly exhibited larger diameter (*$p \leq 0.05$ and **$p \leq 0.01$) compared to monoculture spheroids due to the higher cell viability (≥ 50%). This suggests that coculture spheroids exhibit enhanced resistance to chemotherapeutic agents (Song et al. 2016). 3D-HepG2 spheroids treated with GQD-MSKE-NH_2HMSNs (Figure S7B) maintained over 60% viability, supporting continued proliferation of cancer cells. Accordingly, both monoculture and coculture spheroids increased in diameter over time (Figure S7B). However, in the SNP treated groups, bright-field micrography showed a loss of cellular integrity found in spheroids, indicating an inability to maintain spheroid structure and morphology as seen in Figure S7(C) and by other researchers (Shi et al. 2018; Namgung et al. 2024). Therefore, an increase in 3D-spheroid diameters can reflect both proliferation and toxicity of the cells and cannot be directly used to confirm treatment efficacy. Other complementary assays including viability assay and live-dead cell staining must be employed to elucidate the correct effect.

3.11. Cell death mechanisms

The mechanisms of cell death induced by each treatment were investigated using both apoptotic and lactate dehydrogenase (LDH) assays. The apoptotic assay revealed that MSKE primarily induced early apoptosis in HepG2 cells (****$p \leq 0.0001$, $n = 3$; Figure 13A), which is likely attributable to its main phenolic constituents. In particular, PGG, a key component of MSKE, has been reported to induce apoptosis in HepG2 cells in a concentration-dependent manner (Jiang et al. 2023). GQD-MSKE-NH_2HMSNs also promoted apoptosis (****$p \leq 0.0001$, $n = 3$; Figure 13A), reinforcing the conclusion that apoptosis is the principal mechanism of action for MSKE-based treatments. In contrast, DOX-HMSNs induced late-stage apoptosis, consistent with the well-established mechanism of DOX, which involves several apoptotic events including morphological alterations, phosphatidylserine externalization, and mitochondrial membrane potential collapse (Ye et al. 2007). In addition to late-stage apoptosis, both DOX and DOX-HMSNs exhibited cytotoxic effects that compromised cell membrane integrity. This was evidenced by a significant increase in LDH release from HepG2 cells treated with $1IC_{50}$ of DOX or DOX-HMSNs compared to the untreated control (****$p \leq 0.0001$, $n = 3$; Figure 13B). The SNP treatment resulted in the highest level of total cell death, with a pronounced increase in both late apoptosis and necrosis, indicating an eminent cytotoxic response (Figure 13A). The SNP treatment sequence involved initial incubation with GQD-MSKE-NH_2HMSNs for 6 hours, which induced early apoptosis. Subsequent PTT *via* NIR irradiation and the final treatment with DOX-HMSNs further amplified the cytotoxic effects, leading to elevated late apoptosis and necrosis as major and minor mechanisms, respectively. This combined treatment also significantly disrupted membrane integrity, as confirmed by increased LDH release as seen in Figure 13(B).

The aim of developing the SNP was to enhance HCC treatment through triple combination therapy, integrating an herbal adjuvant, PTT, and chemotherapy. While HCC was developing in chronically damaged liver tissue, COL1 has been abundantly found in fibrotic liver (Yin et al. 2013; Song et al. 2016). Thus, the abundance of COL1 could obstruct drug penetration and decrease the efficacy of treatment. Therefore, the use of PTT was strategically incorporated to reduce COL1 stiffness, facilitating deeper nanoparticle penetration and improving overall therapeutic outcomes. The high therapeutic efficacy of the SNP observed in both 2D and 3D HepG2 models warrants further *in vivo* investigation to validate its anticancer performance under physiological conditions. In this system, GQD-MSKE-NH_2HMSNs were designed to accumulate preferentially in the tumor area toward a passive targeting strategy, providing the initial therapeutic effect *via* MSKE-induced cell death and PTT-mediated ECM modulation. Following this pretreatment phase, DOX-HMSNs were administered and delivered to the same tumor region, where DOX is released from DOX-HMSNs in a pH-responsive manner to kill cancer cells. Notably, neither formulation employed active targeting ligands; therefore, passive targeting *via* the enhanced permeability and retention (EPR) effect and fenestration of tumor blood vessels served as the primary mechanism for the SNP accumulation in tumor tissues (Fang et al. 2011). The nano-size of both GQD-MSKE-NH_2HMSNs and DOX-HMSNs was optimized to exploit this physiological defect of tumor blood vessels for effective tumor localization. Since the GQD-MSKE-NH_2HMSNs had provided prompt release at the first 10 h after the IT administration followed by the sustained release over 48 h. Then, DOX-HMSNs were administered at the same tumor area, the synergy of MSKE-DOX could play their part against HCC. Based on the obtained results and the proposed therapeutic strategy, GQD-MSKE-NH_2HMSNs should be administered *via* intratumoural (IT) injection to ensure localized delivery for effective photothermal therapy (PTT) and adjuvant activity at the tumor site. In contrast, DOX-HMSNs may be administered either through intratumoural (IT) or intravenous (IV) injection, depending on the desired therapeutic coverage.

The IT route enables precise local delivery, reducing off-target effects, and providing high accumulation of GQD-MSKE-NH_2HMSNs and DOX-HMSNs within the tumor area. High local accumulation of GQD-MSKE-NH_2HMSNs is particularly beneficial for subsequent PTT, whereas high accumulation of both GQD-MSKE-NH_2HMSNs and DOX-HMSNs facilitates synergistic anticancer activity of the released MSKE-DOX. To maximize PTT efficacy, key parameters such as laser power, irradiation temperature and penetration depth should be carefully optimized (Cai et al. 2025). Moreover, intratumoural heterogeneity, especially the presence of dense collagen type I (COL1), should be monitored, as it may hinder nanoparticle penetration and limit the therapeutic impact of PTT (Marangon et al. 2017; Peng et al. 2019).

Despite its advantages, the clinical translation of IT delivery is limited by tumor accessibility, and inability to treat metastases (Cai et al. 2025). In contrast, IV administration allows systemic distribution, enabling DOX-HMSNs to accumulate at tumor site through the ERP effects. After IV injection, DOX-HMSNs may be cleared by the mononuclear phagocyte system (MPS) and accumulate in off-target organs, particularly the liver and spleen, raising concerns about systemic toxicity (Blanco et al. 2015). Thus, drug distribution after the administration and toxic effect of drug on major organs must be evaluated during the *in vivo* studies. Once accumulated in the tumor, DOX is released from DOX-HMSNs in response to acidic conditions in the TME. Both GQD-MSKE-NH_2HMSNs and DOX-HMSNs are internalized by cancer cells predominantly through endocytosis, as confirmed by cellular uptake studies. During intracellular trafficking, GQD-MSKE-NH_2HMSNs may escape from endosomes *via* the proton sponge effect, facilitated by their amine surface modification (Gisbert-Garzarán et al. 2021; Basu et al. 2024) allowing the release of MSKE directly into the cytosol, where it can induce apoptosis. Meanwhile, DOX-HMSNs are trafficking to acidic lysosomes, where DOX is released to exert cytotoxic effects on cancer cells.

5. Conclusion

In this study, a novel synergistic interaction between MSKE and DOX was demonstrated in both 2D and 3D-HepG2 monoculture and coculture spheroid models. The anticancer activities of MSKE and DOX were shown to be concentration dependent. Molecular docking analysis revealed that active compounds in MSKE (GA, MGA, and PGG) exhibited strong binding affinities with target proteins such as

EGFR, PIK3CA, TGFβR1, and VEGF, comparable to those of reference inhibitors, thereby elucidating their potential molecular mechanisms of action. To enhance therapeutic efficacy, the SNP was successfully designed and developed. This system, comprising GQD-MSKE-NH_2HMSNs and DOX-HMSNs, provided a triple combination therapy (adjuvant-PTT-chemo) and significantly increased cell death in HepG2 cells through late apoptosis and necrosis, compared to individual treatments. GQD-MSKE-NH_2HMSNs enabled real-time imaging of cellular internalization and effectively reduced collagen type I (COL1) stiffness *via* photothermal therapy (PTT), facilitating MSKE-mediated anticancer activity. Meanwhile, DOX-HMSNs employed the pH-responsive release mechanism and selectively released DOX under acidic TME, thereby reducing the required dose and potentially delaying the onset of drug resistance. In conclusion, the triple combination of herbal adjuvant-induced apoptotic anticancer mechanism, PTT-mediated tumor microenvironment remodeling, and chemotherapeutic cytotoxicity has established the SNP system as a promising nanotheranostic platform for the diagnosis and treatment of HCC.

Acknowledgment

We would like to thank Assist. Prof. Dr. Kuntarat Arunrungvichian for a helpful discussion on drug release.

Authors' contributions

CRediT: **Arunsajee Sae-be**: Data curation, Formal analysis, Investigation, Methodology, Supervision, Validation, Visualization, Writing – original draft, Writing – review & editing; **Jiraporn Leanpolchareanchai**: Formal analysis, Investigation, Methodology, Supervision, Validation, Writing – review & editing; **Piyaporn Plommaithong**: Formal analysis, Investigation, Methodology, Validation, Writing – review & editing; **Apichat Chatsukit**: Formal analysis, Investigation, Methodology, Validation, Writing – review & editing; **Shanapa Ratthanakanungthum**: Formal analysis, Investigation, Methodology, Writing – review & editing; **Kuntida Wongwattanasan**: Formal analysis, Investigation, Methodology, Writing – review & editing; **Tomoki Ota**: Formal analysis, Investigation, Methodology, Writing – review & editing; **Sarunyakorn Raowong**: Investigation, Methodology, Validation, Writing – review & editing; **Pongtip Sithisarn**: Formal analysis, Investigation, Methodology, Supervision, Writing – review & editing; **Savita Chewchinda**: Formal analysis, Investigation, Methodology, Validation, Writing – review & editing; **Parichart Naruphontjirakul**: Formal analysis, Investigation, Methodology, Validation, Writing – review & editing; **Teerasit Termsaithong**: Formal analysis, Investigation, Methodology, Validation, Writing – review & editing; **Thana Sutthibutpong**: Formal analysis, Investigation, Methodology, Supervision, Validation, Writing – review & editing; **Varaporn Buraphacheep Junyaprasert**: Funding acquisition, Resources, Validation, Writing – review & editing; **Khanit Sa-ngiamsuntorn**: Methodology, Resources, Validation, Writing – review & editing; **Rapepol Bavovada**: Investigation, Methodology, Resources, Validation, Writing – review & editing; **Pimolpan Pithayanukul**: Investigation, Methodology, Resources, Validation, Writing – review & editing; **Alexandra E. Porter**: Formal analysis, Investigation, Writing – review & editing; **Pakatip Ruenraroengsak**: Conceptualization, Data curation, Formal analysis, Funding acquisition, Investigation, Methodology, Project administration, Resources, Supervision, Validation, Visualization, Writing – original draft, Writing – review & editing.

Disclosure statement

The authors declare no conflict of interest.

Funding

This work was sponsored by the Program Management Unit for Human Resources & Institutional Development, Research and Innovation, NXPO (grant number B05F630058), Mahidol University—New Discovery and Frontier Research Fund (grant number 64A11), Mahidol University (Fundamental Fund: fiscal year 2024 (FF-042/2567) by National Science Research and Innovation Fund (NSRF)) and the Thailand Research Fund (TRF). AS was supported through the Royal Golden Jubilee Ph.D. Program (RGJ-PHD, grant number PHD/0070/2561) by National Research Council of Thailand (NRCT). SR was supported through the Royal Golden Jubilee Ph.D. Program (RGJ-PHD, grant number N41A650105) by National Research Council of Thailand (NRCT).

Data availability statement

All data supporting the results of this study are available from the article and its supplementary information or from the corresponding author upon reasonable request. A reporting summary for this Article is available as a Supplementary Information file. Source data is provided in this paper.

References

Abdullah A-SH, Mohammed AS, Rasedee A, Mirghani MES. 2015. Oxidative stress-mediated apoptosis induced by ethanolic mango seed extract in cultured estrogen receptor positive breast cancer MCF-7 cells. Int J Mol Sci. 16(2):3528–3536. doi: 10.3390/ijms16023528.

Arnold F, Muzzio N, Patnaik SS, Finol EA, Romero G. 2021. Pentagalloyl glucose-laden poly(lactide-co-glycolide) nanoparticles for the biomechanical extracellular matrix stabilization of an in vitro abdominal aortic aneurysm model. ACS Appl Mater Interf. 13(22):25771–25782. doi: 10.1021/acsami.1c05344.

Aryal S, Baniya MK, Danekhu K, Kunwar P, Gurung R, Koirala N. 2019. Total phenolic content, flavonoid content and antioxidant potential of wild vegetables from western Nepal. Plants. 8(4):96. doi: 10.3390/plants8040096.

Basu A, Sae-be A, Namporn T, Suriyaphan O, Sithisarn P, Leanpolchareanchai J, Plommaithong P, Chatsukit A, Sa-Ngiamsuntorn K, Naruphontjirakul P, et al. 2024. Delivery of avocado seed extract using novel charge-switchable mesoporous silica nanoparticles with galactose surface modified to target sorafenib-resistant hepatocellular carcinoma. Int J Nanomed. 19:10341–10365. doi: 10.2147/IJN.S478574.

Berman HM, Westbrook J, Feng Z, Gilliland G, Bhat TN, Weissig H, Shindyalov IN, Bourne PE. 2000. The protein data bank. Nucleic Acid Res. 28(1):235–242. doi: 10.1093/nar/28.1.235.

Bhatt HN, Diwan R, Borrego EA, Pérez CAM, Varela-Ramirez A, Kumar R, Aguilera RJ, Nurunnabi M. 2023. A photothermal driven chemotherapy for the treatment of metastatic melanoma. J Control Release. 361:314–333. doi: 10.1016/j.jconrel.2023.08.005.

Blanco E, Shen H, Ferrari M. 2015. Principles of nanoparticle design for overcoming biological barriers to drug delivery. Nat Biotechnol. 33(9):941–951. doi: 10.1038/nbt.3330.

Bold G, Schnell C, Furet P, McSheehy P, Brüggen J, Mestan J, Manley PW, Drückes P, Burglin M, Dürler U, et al. 2016. A novel potent oral series of VEGFR2 inhibitors abrogate tumor growth by inhibiting angiogenesis. J Med Chem. 59(1):132–146. doi: 10.1021/acs.jmedchem.5b01582.

Cai Y, Chai T, Nguyen W, Liu J, Xiao E, Ran X, Ran Y, Du D, Chen W, Chen X, et al. 2025. Phototherapy in cancer treatment: strategies and challenges. Signal Transduct Target Ther. 10(1):115. doi: 10.1038/s41392-025-02140-y.

Chen F, Hong H, Shi S, Goel S, Valdovinos HF, Hernandez R, Theuer CP, Barnhart TE, Cai W. 2014. Engineering of hollow mesoporous silica nanoparticles for remarkably enhanced tumor active targeting efficacy. Sci Rep. 4(1):5080. doi: 10.1038/srep05080.

Chen T, Yu H, Yang N, Wang M, Ding C, Fu J. 2014. Graphene quantum dot-capped mesoporous silica nanoparticles through an acid-cleavable acetal bond for intracellular drug delivery and imaging. J Mater Chem B. 2(31):4979–4982. doi: 10.1039/c4tb00849a.

Chong Y, Ma Y, Shen H, Tu X, Zhou X, Xu J, Dai J, Fan S, Zhang Z. 2014. The in vitro and in vivo toxicity of graphene quantum dots. Biomaterials. 35(19):5041–5048. doi: 10.1016/j.biomaterials.2014.03.021.

Chou TC. 2010. Drug combination studies and their synergy quantification using the Chou-Talalay method. Cancer Res. 70(2):440–446. doi: 10.1158/0008-5472.CAN-09-1947.

Dar MS, Tabish TA, Thorat ND, Swati G, Sahu NK. 2023. Photothermal therapy using graphene quantum dots. APL Bioeng. 7(3):031502. doi: 10.1063/5.0160324.

Department of Medical Sciences (DMSc). 2020. Thai Herbal Pharmacopoeia II supplement. Ministry of Public Health. URL: https://www.bdn.go.th/tp/ebook. Accessed: March 29, 2024.

Dong Y, Yin S, Jiang C, Luo X, Guo X, Zhao C, Fan L, Meng Y, Lu J, Song X, et al. 2014. Involvement of autophagy induction in penta-1,2,3,4,6-O-galloyl-β-D-glucose-induced senescence-like growth arrest in human cancer cells. Autophagy. 10(2):296–310. doi: 10.4161/auto.27210.

Eberhardt J, Santos-Martins D, Tillack AF, Forli S. 2021. AutoDock Vina 1.2.0: new docking methods, expanded force field, and python bindings. J Chem Inf Model. 61(8):3891–3898. doi: 10.1021/acs.jcim.1c00203.

Ediriwickrema A, Zhou J, Deng Y, Saltzman WM. 2014. Multi-layered nanoparticles for combination gene and drug delivery to tumors. Biomaterials. 35(34):9343–9354. doi: 10.1016/j.biomaterials.2014.07.043.

European Association for the Study of the Liver (EASL). 2018. EASL clinical practice guidelines: management of hepatocellular carcinoma. J Hepatol. 69:182–236.

Ezzati N, Mahjoub AR, Abolhosseini Shahrnoy A, Syrgiannis Z. 2019. Amino acid-functionalized hollow mesoporous silica nanospheres as efficient biocompatible drug carriers for anticancer applications. Int J Pharm. 572:118709. doi: 10.1016/j.ijpharm.2019.118709.

Fang J, Nakamura H, Maeda H. 2011. The EPR effect: unique features of tumor blood vessels for drug delivery, factors involved, and limitations and augmentation of the effect. Adv Drug Dev Rev. 63:136–151.

Ferlay J, Ervil M, Lam F, et al. 2022. Global cancer observatory (Globocan 2022): cancer today. Lyon, France: International Agency for Research on Cancer. World Health Organization (WHO). URL: https://gco.iarc.who.int/today. accessed: March 29, 2024.

Gao Y, Chen Y, Ji X, He X, Yin Q, Zhang Z, Shi J, Li Y. 2011. Controlled intracellular release of doxorubicin in multidrug-resistant cancer cells by tuning the shell-pore sizes of mesoporous silica nanoparticles. ACS Nano. 5(12):9788–9798. doi: 10.1021/nn2033105.

Gisbert-Garzarán M, Lozano D, Matsumoto K, Komatsu A, Manzano M, Tamanoi F, Vallet-Regí M. 2021. Designing mesoporous silica nanoparticles to overcome biological barriers by incorporating targeting and endosomal escape. ACS Appl Mater Interf. 13(8):9656–9666. doi: 10.1021/acsami.0c21507.

Greasley SL, Page SJ, Sirovica S, Chen S, Martin RA, Riveiro A, Hanna JV, Porter AE, Jones JR. 2016. Controlling particle size in the Stöber process and incorporation of calcium. J Colloid Interface Sci. 469:213–223. doi: 10.1016/j.jcis.2016.01.065.

He X, Yang Y, Han Y, Cao C, Zhang Z, Li L, Xiao C, Guo H, Wang L, Han L, et al. 2023. Extracellular matrix physical properties govern the diffusion of nanoparticles in tumor microenvironment. Proc Natl Acad Sci U S A. 120(1):e2209260120. doi: 10.1073/pnas.2209260120.

Huang C-Y, Chang Y-J, Wei P-L, Hung C-S, Wang W. 2021. Methyl gallate, gallic acid-derived compound, inhibit cell proliferation through increasing ROS production and apoptosis in hepatocellular carcinoma cells. PLoS One. 16(3):e0248521. doi: 10.1371/journal.pone.0248521.

Huang H, Shao L, Chen Y, Han W, Zhou Y, Liu T, Gu J, Zhu H. 2022. Sequential dual delivery system based on siCOX-2-loaded gold nanostar and thermal-sensitive liposomes overcome hypoxia-mediated multidrug resistance in tumors. Mol Pharm. 19(7):2390–2405. doi: 10.1021/acs.molpharmaceut.2c00164.

Humphrey W, Dalke A, Schulten K. 1996. VMD: visual molecular dynamics. J Mol Graph. 14(1):33–38. doi: 10.1016/0263-7855(96)00018-5.

Issels RD. 2008. Hyperthermia adds to chemotherapy. Eur J Cancer. 44(17):2546–2554. doi: 10.1016/j.ejca.2008.07.038.

Jiamboonsri P, Pithayanukul P, Bavovada R, Leanpolchareanchai J, Yin T, Gao S, Hu M. 2015. Factors influencing oral bioavailability of Thai Mango seed kernel extracts and its key phenolic principles. Molecules. 20(12):21254–21273. doi: 10.3390/molecules201219759.

Jiang Y-H, Bi J-H, Wu M-R, Ye S-J, Hu L, Li L-J, Yi Y, Wang H-X, Wang L-M. 2023. In vitro anti-hepatocellular carcinogenesis of 1,2,3,4,6-penta-O-gallyoyl-β-D-glucose. Food Nutr Res. 67:9244. doi: 10.29219/fnr.v67.9244.

Kant R, Yen C-H, Hung J-H, Lu C-K, Tung C-Y, Chang P-C, Chen Y-H, Tyan Y-C, Chen Y-MA. 2019. Induction of GNMT by 1,2,3,4,6-penta-O-galloyl-beta-D-glucopyranoside through proteasome-independent MYC downregulation in hepatocellular carcinoma. Sci Rep. 9(1):1968. doi: 10.1038/s41598-018-37292-1.

Kant R, Yen C-H, Lu C-K, Lin Y-C, Li J-H, Chen Y-MA. 2016. Identification of 1,2,3,4,6-Penta-O-galloyl-β-D-glycopyranoside as a Glycine N-Methyltransferase enhancer by high-throughput screening of natural products inhibits hepatocellular carcinoma. Int J Mol Sci. 17(5):669. doi: 10.3390/ijms17050669.

Kim T-H, Mount CW, Gombotz WR, Pun SH. 2010. The delivery of doxorubicin to 3-D multicellular spheroids and tumors in a murine xenograft model using tumor-penetrating triblock polymeric micelles. Biomater. 31(28):7386–7397. doi: 10.1016/j.biomaterials.2010.06.004.

Kong M, Tang J, Qiao Q, Wu T, Qi Y, Tan S, Gao X, Zhang Z. 2017. Biodegradable hollow mesoporous silica nanoparticles for regulating tumor microenvironment and enhancing antitumor efficiency. Theranostics. 7(13):3276–3292. doi: 10.7150/thno.19987.

Laskowski RA, Swindells MB. 2011. LigPlot+: multiple ligand–protein interaction diagrams for drug discovery. J Chem Inf Model. 51(10):2778–2786. doi: 10.1021/ci200227u.

Latimer GW. 2019. AOAC official method. 21st ed. Gaithersburg, MD: AOAC International.

Leanpolchareanchai J, Padois K, Falson F, Bavovada R, Pithayanukul P. 2014. Microemulsion system for topical delivery of Thai mango seed kernel extract: development, physicochemical characterization and ex vivo skin permeation studies. Molecules. 19(11):17107–17129. doi: 10.3390/molecules191117107.

Lee SM, Papathakis ML, Feng H-MC, Hunter GF, Carr JE. 1991. Multipesticide residue method for fruits and vegetables: California department of food and agriculture. Fresenius J Anal Chem. 339(6):376–383. doi: 10.1007/BF00322352.

Liang H, Chen Z, Yang R, Huang Q, Chen H, Chen W, Zou L, Wei P, Wei S, Yang Y, et al. 2022. Methyl gallate suppresses the migration, invasion, and epithelial-mesenchymal transition of hepatocellular carcinoma cells via the AMPK/NF-κB signaling pathway in vitro and in vivo. Front Pharmacol. 13:894285. doi: 10.3389/fphar.2022.894285.

Lima KG, Krause GC, Schuster AD, Catarina AV, Basso BS, De Mesquita FC, Pedrazza L, Marczak ES, Martha BA, Nunes FB, et al. 2016. Gallic acid reduces cell growth by induction of apoptosis and reduction of IL-8 in HepG2 cells. Biomed Pharmacother. 84:1282–1290. doi: 10.1016/j.biopha.2016.10.048.

Lin S-R, Chang C-H, Hsu C-F, Tsai M-J, Cheng H, Leong MK, Sung P-J, Chen J-C, Weng C-F. 2020. Natural compounds as potential adjuvants to cancer therapy: preclinical evidence. Br J Pharmacol. 177(6):1409–1423. doi: 10.1111/bph.14816.

Liu J, Luo Z, Zhang J, Luo T, Zhou J, Zhao X, Cai K. 2016. Hollow mesoporous silica nanoparticles facilitated drug delivery via cascade pH stimuli in tumor microenvironment for tumor therapy. Biomaterials. 83:51–65. doi: 10.1016/j.biomaterials.2016.01.008.

Liu X, Jiang J, Chan R, Ji Y, Lu J, Liao Y-P, Okene M, Lin J, Lin P, Chang CH, et al. 2019. Improved efficacy and reduced toxicity using a custom-designed irinotecan-delivering silicasome for orthotopic colon cancer. ACS Nano. 13(1):38–53. doi: 10.1021/acsnano.8b06164.

Llovet JM, Kelley RK, Villanueva A, Singal AG, Pikarsky E, Roayaie S, Lencioni R, Koike K, Zucman-Rossi J, Finn RS, et al. 2021. Hepatocellular carcinoma. Nat Rev Dis Primers. 7(1):6. doi: 10.1038/s41572-020-00240-3.

Loescher CM, Morton DW, Razic S, Agatonovic-Kustrin S. 2014. High performance thin layer chromatography (HPTLC) and high performance liquid chromatography (HPLC) for the qualitative and quantitative analysis of Calendula officinalis-Advantages and limitations. J Pharm Biomed Anal. 98:52–59. doi: 10.1016/j.jpba.2014.04.023.

Luo F, Fu Y, Xiang Y, Yan S, Hu G, Huang X, Huang G, Sun C, Li X, Chen K, et al. 2014. Identification of quantification of gallotannins in mango (*Mangifera indica* L.) kernel and peel and their antiproliferative activities. J Funct Food. 8:282–291. doi: 10.1016/j.jff.2014.03.030.

Mandelker D, Gabelli SB, Schmidt-Kittler O, Zhu J, Cheong I, Huang C-H, Kinzler KW, Vogelstein B, Amzel LM. 2009. A frequent kinase domain mutation that changes the interaction between PI3Kα and the membrane. Proc Natl Acad Sci U S A. 106(40):16996–17001. doi: 10.1073/pnas.0908444106.

Marangon I, Silva AAK, Guilbert T, Kolosnjaj-Tabi J, Marchiol C, Natkhunarajah S, Chamming's F, Ménard-Moyon C, Bianco A, Gennisson J-L, et al. 2017. Tumor stiffening, a key determinant of tumor progression, is reversed by nanomaterial-induced photothermal therapy. Theranostics. 7(2):329–343. doi: 10.7150/thno.17574.

Mirza B, Croley CR, Ahmad M, Pumarol J, Das N, Sethi G, Bishayee A. 2021. Mango (*Mangifera indica* L.): a magnificent plant with cancer preventive and anticancer therapeutic potential. Crit Rev Food Sci Nutr. 61(13):2125–2151. doi: 10.1080/10408398.2020.1771678.

Moghaddam SPH, Yazdimamaghani M, Ghandehari H. 2018. Glutathione-sensitive hollow mesoporous silica nanoparticles for controlled drug delivery. J Control Release. 282:62–75.

Namgung B, Dai H, Prathyushaa Vikraman P, Saha T, Sengupta S, Lin Jang H. 2024. An inexpensive "do-it-yourself" device for rapid generation of uniform tumor spheroids. Device. 2(3):100255. doi: 10.1016/j.device.2024.100255.

Nithitanakool S, Pithayanukul P, Bavovada R. 2009. Antioxidant and hepatoprotective activities of Thai mango seed kernel extract. Planta Med. 75(10):1118–1123. doi: 10.1055/s-0029-1185507.

Peng J, Yang Q, Shi K, Xiao Y, Wei X, Qian Z. 2019. Intratumoral fate of functional nanoparticles in response to microenvironment factor: implications on cancer diagnosis and therapy. Adv Drug Deliv Rev. 143:37–67. doi: 10.1016/j.addr.2019.06.007.

Pinna A, Torki Baghbaderani M, Vigil Hernández V, Naruphontjirakul P, Li S, McFarlane T, Hachim D, Stevens MM, Porter AE, Jones JR, et al. 2021. Nanoceria provides antioxidant and osteogenic properties to mesoporous silica nanoparticles for osteoporosis treatment. Acta Biomater. 122:365–376. doi: 10.1016/j.actbio.2020.12.029.

Priwitaningrum DL, Blondé J-BG, Sridhar A, van Baarlen J, Hennink WE, Storm G, Le Gac S, Prakash J. 2016. Tumor stroma-containing 3D spheroid arrays: a tool to study nanoparticle penetration. J Control Release. 244(Pt B):257–268. doi: 10.1016/j.jconrel.2016.09.004.

Sae-be A, Wiwatpanit T, Varatthan T, Namporn T, Laungkulldej S, Thiabma R, Jaiboonma A, Sa-ngiamsuntorn K, Elson D, Porter AE, et al. 2023. Comparative study between the 3D-liver spheroid models developed from HepG2 and immortalized hepatocyte-like cells with primary hepatic stellate coculture for drug metabolism analysis and anticancer drug screening. Adv Therap. 6:2200169.

Sa-Ngiamsuntorn K, Wongkajornsilp A, Kasetsinsombat K, Duangsa-Ard S, Nuntakarn L, Borwornpinyo S, Akarasereenont P, Limsrichamrern S, Hongeng S. 2011. Upregulation of CYP 450s expression of immortalized hepatocyte-like cells derived from mesenchymal stem cells by enzyme inducers. BMC Biotechnol. 11(1):89. doi: 10.1186/1472-6750-11-89.

Sawyer JS, Beight DW, Britt KS, Anderson BD, Campbell RM, Goodson TJr, Herron DK, Li HY, McMilliam WT, Mort N, et al. 2004. Synthesis and activity of new aryl- and heteroaryl-substituted 5,6-dihydro-4H-pyrrolo[1,2-b]pyrazole inhibitors of the transforming growth factor-beta type I receptor kinase domain. BMCL. 14:3581–3584.

Shaban NZ, El-Rashidy FH, Adam AH, Beltagy DM, Ali AE, Abde-Alaziz AA, Talaat IM. 2023. Anticancer role of mango (*Mangifera indica* L.) peel and seed kernel extracts against 7,12- dimethylbenz[a] anthracene-induced mammary carcinogenesis in female rats. Sci Rep. 13(1):7703. doi: 10.1038/s41598-023-34626-6.

Shi C-J, Zheng Y-B, Pan F-F, Zhang F-W, Zhuang P, Fu W-M. 2021. Gallic acid suppressed tumorigenesis by a LncRNA MALAT1-Wnt/β-Catenin axis in hepatocellular carcinoma. Front Pharmacol. 12:708967. doi: 10.3389/fphar.2021.708967.

Shi W, Kwon J, Huang Y, Tan J, Uhl CG, He R, Zhou C, Liu Y. 2018. Facile tumor spheroids formation in large quantity with controllable size and high uniformity. Sci Rep. 8(1):6837. doi: 10.1038/s41598-018-25203-3.

Shim G, Kim M-G, Kim D, Park JY, Oh Y-K. 2017. Nanoformulation-based sequential combination cancer therapy. Adv Drug Deliv Rev. 115:57–81. doi: 10.1016/j.addr.2017.04.003.

Singal AG, Kanwal F, Llovet JM. 2023. Global trends in hepatocellular carcinoma epidemiology: implications for screening, prevention and therapy. Nat Rev Clin Oncol. 20(12):864–884. doi: 10.1038/s41571-023-00825-3.

Sogi DS, Siddiq M, Greiby I, Dolan KD. 2013. Total phenolics, antioxidant activity, and functional properties of 'Tommy Atkins' mango peel and kernel as affected by drying methods. Food Chem. 141(3):2649–2655. doi: 10.1016/j.foodchem.2013.05.053.

Song Y, Kim S-H, Kim KM, Choi EK, Kim J, Seo HR. 2016. Activated hepatic stellate cells play pivotal roles in hepatocellular carcinoma cell chemoresistance and migration in multicellular tumor spheroids. Sci Rep. 6(1):36750. doi: 10.1038/srep36750.

Stamos J, Sliwkowski MX, Eigenbrot C. 2002. Structure of the epidermal growth factor receptor kinase domain alone and in complex with a 4-anilinoquinazoline inhibitor. J Biol Chem. 277(48):46265–46272. doi: 10.1074/jbc.M207135200.

Wu SH, Mou CY, Lin HP. 2013. Synthesis of mesoporous silica nanoparticles. Chem Soc Rev. 42(9):3862–3875. doi: 10.1039/c3cs35405a.

Xia H, Dai X, Yu H, Zhou S, Fan Z, Wei G, Tang Q, Gong Q, Bi F. 2018. EGFR-PI3K-PDK1 pathway regulates YAP signaling in hepatocellular carcinoma: the mechanism and its implications in targeted therapy. Cell Death Dis. 9(3):269. doi: 10.1038/s41419-018-0302-x.

Yang JD, Hainaut P, Gores GJ, Amadou A, Plymoth A, Roberts LR. 2019. A global view of hepatocellular carcinoma: trends, risk, prevention and management. Nat Rev Gastroenterol Hepatol. 16(10):589–604. doi: 10.1038/s41575-019-0186-y.

Yao X, Tian Z, Liu J, Zhu Y, Hanagata N. 2017. Mesoporous silica nanoparticles capped with graphene quantum dots for potential chemo-photothermal synergistic cancer therapy. Langmuir. 33(2):591–599. doi: 10.1021/acs.langmuir.6b04189.

Ye N, Qin J, Liu X, Shi W, Lin B. 2007. Characterizing doxorubicin-induced apoptosis in HepG2 cells using an integrated microfluidic device. Electrophoresis. 28(7):1146–1153. doi: 10.1002/elps.200600450.

Yin C, Evason KJ, Asahina K, Stainier DYR. 2013. Hepatic stellate cells in liver development, regeneration, and cancer. J Clin Invest. 123(5):1902–1910. doi: 10.1172/JCI66369.

Yoopum S, Wongmanee N, Rojanaverawong W, Rattanapunya S, Sumsakul W, Hanchang W. 2023. Mango (*Mangifera indica* L.) seed kernel extract suppresses hyperglycemia by modulating pancreatic β cell apoptosis and dysfunction and hepatic glucose metabolism in diabetic rats. Environ Sci Pollut Res Int. 30(59):123286–123308. doi: 10.1007/s11356-023-31066-7.

Zhang Z, Wang J, Nie X, Wen T, Ji Y, Wu X, Zhao Y, Chen C. 2014. Near infrared laser-induced targeted cancer therapy using thermoresponsive polymer encapsulated gold nanorods. J Am Chem Soc. 136(20):7317–7326. doi: 10.1021/ja412735p.